

Global analysis of data on the spin-orbit-coupled $A^1\Sigma_u^+$ and $b^3\Pi_u$ states of Cs_2

Jianmei Bai, E. H. Ahmed, B. Beser, Y. Guan, S. Kotochigova, and A. M. Lyyra
Physics Department, Temple University, Philadelphia, Pennsylvania 19122, USA

S. Ashman,^{*} C. M. Wolfe,[†] and J. Huennekens
Department of Physics, Lehigh University, Bethlehem, Pennsylvania 18015, USA

Feng Xie, Dan Li,[‡] and Li Li
Department of Physics and Key Lab of Atomic and Molecular Nanoscience, Tsinghua University, Beijing 100084, China

M. Tamanis and R. Ferber
Laser Center, Department of Physics, University of Latvia, 19 Rains Blvd., Riga LV-1586, Latvia

A. Drozdova, E. Pazyuk, and A. V. Stoloyarov[§]
Department of Chemistry, Moscow State University, GSP-2 Leninskie gory 1/3, Moscow RU-119992, Russia

J. G. Danzl and H.-C. Nägerl
Institut für Experimentalphysik und Zentrum für Quantenphysik, Universität Innsbruck, Technikerstrasse 25, A-6020 Innsbruck, Austria

N. Bouloufa, O. Dulieu, and C. Amiot^{||}
Laboratoire Aimé Cotton, CNRS, Université Paris-Sud, Bât. 505, F-91405 Orsay Cedex, France

H. Salami[¶] and T. Bergeman
Department of Physics and Astronomy, SUNY, Stony Brook, New York 11794-3800, USA
 (Received 23 December 2010; published 28 March 2011)

We present experimentally derived potential curves and spin-orbit interaction functions for the strongly perturbed $A^1\Sigma_u^+$ and $b^3\Pi_u$ states of the cesium dimer. The results are based on data from several sources. Laser-induced fluorescence Fourier transform spectroscopy (LIF FTS) was used some time ago in the Laboratoire Aimé Cotton primarily to study the $X^1\Sigma_g^+$ state. More recent work at Tsinghua University provides information from moderate resolution spectroscopy on the lowest levels of the $b^3\Pi_{0u}^\pm$ state as well as additional high-resolution data. From Innsbruck University, we have precision data obtained with cold Cs_2 molecules. Recent data from Temple University was obtained using the optical-optical double resonance polarization spectroscopy technique, and finally, a group at the University of Latvia has added additional LIF FTS data. In the Hamiltonian matrix, we have used analytic potentials (the expanded Morse oscillator form) with both finite-difference (FD) coupled-channel and discrete variable representation (DVR) calculations of the term values. Fitted diagonal and off-diagonal spin-orbit functions are obtained and compared with *ab initio* results from Temple and Moscow State universities.

DOI: [10.1103/PhysRevA.83.032514](https://doi.org/10.1103/PhysRevA.83.032514)

PACS number(s): 33.20.Kf, 31.15.aj, 31.50.Df

I. INTRODUCTION

The lowest electronically excited states of alkali-metal dimers have long been of interest as gateway or “window” states for the excitation of higher singlet or triplet levels

[1]. Quite recently, various low excited states of alkali-metal dimers have also been used as intermediaries in the production of ultracold molecules, as for RbCs [2], LiCs [3], KRb [4–6], NaCs [7], Rb₂ [8], and Cs₂ [9–14]. Although molecules with electric dipole moments have attracted the most interest, homonuclear species, such as Cs₂, also offer the interesting conceptual challenge of nonspherically symmetric particles in a condensate [15]. Furthermore the cold atoms can be prepared with fewer lasers than required for dual species systems. Cold Cs₂ molecules may also be useful in experiments designed to be sensitive to the electron:proton mass ratio, as discussed in [16].

Various new possibilities inherent in cold molecules have prompted efforts to obtain and analyze the spectra of alkali-metal dimer molecules. The lowest excited states above the $^2S+^2S$ limit, namely the $A^1\Sigma_{(u)}^+$ and $b^3\Pi_{(u)}$ states (where the ungerade designation applies only to homonuclear

^{*}Present address: Department of Physics and Astronomy, University of Wisconsin – Stevens Point, Stevens Point, WI 54481.

[†]Present address: Army Research Laboratory, RDRL-WMP-A, Aberdeen Proving Ground, MD 21005-5066.

[‡]Present address: State Key Laboratory of Precision Spectroscopy and Department of Physics, East China Normal University, Shanghai 200062.

[§]avstol@phys.chem.msu.ru

^{||}Retired from LAC.

[¶]Present address: Department of Physics, Faculty of Sciences (V), Lebanese University, Nabatieh, Lebanon.

species), would seem to be especially interesting in this regard. However, transitions from the ground state may require frequencies for which the availability of laser sources is limited. Furthermore, spin-orbit perturbative interactions between the A - b state levels complicate the spectra. As a route to cold ground-state molecules from weakly bound molecules that are formed on a predominantly triplet Feshbach resonance (FR), the A - b states of homonuclear species do not have the special advantage of possible triplet to singlet transfer which is possible in heteronuclear species [17] for which the dipole selection rule that forbids *ungerade* to *ungerade* radiative transitions in homonuclear species does not apply. In view of these difficulties, it is worth noting that, to date, only for Cs_2 have the A - b states been used as intermediates in the production of cold molecules [11–14]. The spin-orbit perturbations are somewhat more severe in species containing Rb or Cs than in the A - b states of other alkali-metal dimers. Nevertheless, with Cs_2 , Refs. [11–14] used the $X^1\Sigma_g^+$ component of a weakly bound molecule formed on a FR to excite to the $A^1\Sigma_u^+$ component of an upper state level. Two two-photon steps were used to efficiently connect the FR molecular state, via $X(v=73, J=2)$ to $X(v=0, J=0)$.

Recently, the methods available for analyzing and modeling spectroscopic data on highly perturbed states have been extended [18–27]. As is evident from the discussion below, each effort to perform a “global analysis” of all available data on these two electronic states raises additional questions about what Hamiltonian elements and functions are required, and what data are required to determine the parameters so as to achieve a fit with residuals comparable to experimental uncertainties. There has been impressive progress in data acquisition and analysis for the heteronuclear A - b states from work on NaK [28–32] to more recent work on NaRb [19,23], NaCs [24], KCs [25,26], and RbCs [21,27]. For NaRb, NaCs, and KCs, vibrational assignments of both states have been reliably determined, and the perturbative interactions have been modeled to an accuracy of 0.01 cm^{-1} or better. Higher-order spin-orbit effects were included in [24] and [25], and there was quite good agreement between empirically extracted and *ab initio* potentials. Curiously, for one alkali-metal dimer recently used for cold molecule work, namely KRb [4,5], spectroscopic data on low levels of the $A^1\Sigma^+$ and $b^3\Pi$ states appear to be lacking, and optical state transfer processes leading to cold KRb molecules have used other pathways.

There have also been a succession of studies of the A - b states of the lighter homonuclear alkali-metal dimer species Li_2 [33–36], Na_2 [22,37–41], K_2 [18,20,42–46], and Rb_2 [47,48]. For Na_2 [22], data now extend almost continuously from the lowest vibrational levels to the atomic limit.

One question that arises when considering this summary of spectroscopic data on the A - b states of Cs_2 is why hyperfine structure (hfs) is not reported. Earlier work [37] on the A - b states of Na_2 , using a molecular beam, and accessing levels with significant $^3\Pi_{2u}$ character, showed hfs structure spanning several hundred MHz. The atomic hfs interaction of ^{133}Cs is larger than that of ^{23}Na . Two of the techniques in the present work, namely optical-optical double resonance polarization spectroscopy and spectroscopy with cold ground-state Cs_2 molecules, have very small inherent

linewidths. Nevertheless, the transitions observed here are not expected to exhibit hyperfine structure, as we discuss in Sec. VI below.

This paper presents a detailed model of the energy-level structure of the A - b states of Cs_2 . In Sec. II, we describe experimental techniques used to obtain high-resolution spectra. Section III describes the model used to fit the data. Section IV discusses present *ab initio* results for potentials and spin-orbit functions, calculated from two different approaches. Section V discusses radiative properties of the A - b complex, including certain anomalies occurring for mixed singlet-triplet upper states. Section VI discusses the possibilities for observing hyperfine structure, while Sec. VII gives a short summary and conclusion.

II. THE EXPERIMENTAL DATA

This report combines experimental data from several sources. A substantial part comes from Fourier transform spectroscopy (FTS) performed in the Laboratoire Aimé Cotton (LAC), Orsay, France, in connection with the study of the Cs_2 $X^1\Sigma_g^+$ ground state as presented in [49,50]. More recently, FTS data have been obtained at the University of Latvia in Riga. Additional high-resolution data were obtained in Tsinghua University, Beijing, using fluorescence excitation spectroscopy. Another valuable component of the data consists of fluorescence lines from the $2^3\Delta_{1g}$ state [51], observed at Tsinghua University, which provided information on the lowest vibrational levels of the $b^3\Pi_{0u}$ state, of both parities, $\pm(-1)^J$. An ultra-high-resolution data set, limited in absolute accuracy by wavelength meter calibration, was obtained by excitation of cold Cs_2 molecules at the University of Innsbruck, covering a limited range of energies. Finally, because of a substantial gap in the above data on higher A - b levels, the Lyyra and Huennekens groups, working at Temple University, employed optical-optical double resonance (OODR) polarization spectroscopy, with collisional orientation transfer as in [48], to partially fill in this gap. Unlike the other data sets, the work at Temple has not been published previously and therefore the discussion is more detailed.

A. Data from Fourier transform spectroscopy

Many of the term values used in the present work are the upper state levels from transitions observed in LAC and reported in [49] and [50]. Cs atoms in a heat pipe oven at 600 K were excited, in the 1987 study by an argon-ion laser, and in the 2002 work by a titanium-doped sapphire laser, pumped by an argon-ion laser. The fluorescence in the backward direction was collected and sent into a Fourier spectrometer with a 2-m optical path length difference. Wave numbers were calibrated by reference to a xenon atomic transition near $3.5\text{ }\mu\text{m}$, with absolute uncertainties between 0.001 and 0.003 cm^{-1} . For [50], 16 900 transitions were measured from 113 main fluorescence series and 348 series including rotational relaxation. The data are no longer available on the LAC website, but are posted in the supplemental material file associated with this article [52].

At the University of Latvia, FTS data on the A - b states of Cs_2 have been obtained recently in the process of analyzing

the $A-b \rightarrow X$ laser-induced fluorescence (LIF) spectra of KCs [25,26] and RbCs [27] molecules. In these spectra, along with transitions in KCs and RbCs, the $A-b \rightarrow X$ LIF spectra of Cs₂ molecules were present as well. In the experiments, the molecules were produced in a linear heat-pipe at about 565 K temperature and excited by diode lasers centered at 980 nm, 1020 nm, and 1050 nm. The backward LIF spectra have been recorded by Fourier transform spectrometer IFS-125HR with 0.03 cm⁻¹ resolution. The transition frequencies obtained, with ca. 0.003–0.004 cm⁻¹ accuracy, have been added to the X -state term values of Cs₂ calculated with the X -state potential of [50], corrected by [53]. The estimated overall uncertainty of term values, accounting for Doppler broadening, is about 0.01 cm⁻¹.

The relative LIF intensity distributions have been determined in sufficiently lengthy progressions, accounting for the spectral sensitivity of the InGaAs detector as described in Ref. [25]. For comparison with theory, the intensities were averaged over P, R doublet components and corrected for the spectral sensitivity of the detector.

B. Fluorescence excitation spectroscopy

This approach, employed at Tsinghua University, involved two-photon excitation to a higher state ($^3\Pi_g$ or $^3\Delta_g$) from levels of the $X^1\Sigma_g^+$ state via levels of the $A^1\Sigma_u^+$ state, which was monitored by observing decay (direct or collision-induced) to the $a^3\Sigma_u^+$ state. After the double resonance signal was found and optimized, the same $3^3\Pi_g(v, J = J' + 1)$ [or $2^3\Delta_g(v, J = J' + 1)$] or $3^3\Pi_g(v, J = J' - 1)$ [or $2^3\Delta_g(v, J = J' - 1)$] upper level was excited from $A^1\Sigma_u^+(v', J' + 2)$ or $A^1\Sigma_u^+(v', J' - 2)$ intermediate levels. Thus the term values of the $A^1\Sigma_u^+(v', J' + 2)$ or $A^1\Sigma_u^+(v', J' - 2)$ levels can be obtained by adding the term values of the $X^1\Sigma_g^+(v'', J'' = J' + 1, \text{ or } J' + 3)$ or $X^1\Sigma_g^+(v'', J'' = J' - 1, \text{ or } J' - 3)$ ground levels [50] to the pump-laser frequency with an accuracy of ~ 0.003 cm⁻¹.

C. Spectroscopic observations on cold Cs₂ molecules

As part of the effort at the University of Innsbruck to produce ultracold Cs₂ molecules in the rovibronic ground state near quantum degeneracy [11,14], weakly bound molecules were formed by association of atoms on a Feshbach resonance in a high phase-space density sample. Subsequently, two STIRAP transitions were used to transfer the population to $X(v = 0)$. A first pair of lasers linked the Feshbach level to the intermediate level, $X(v = 73, J = 0 \text{ or } J = 2)$, via an $A-b$ excited state level near 12 500 cm⁻¹. Unfortunately, in the present study there were insufficient data points near the levels around 12 500 cm⁻¹, so these term values could not be accurately fit in our analysis.

The second two-photon transition starting from the $X(v = 73)$ level involved an $A-b$ intermediate level near 10 000 cm⁻¹. Spectroscopy on the first transition, as described in detail in Ref. [13], was carried out by irradiating the Feshbach molecules for a given time with light near 1126 nm, stepping the laser frequency with each cycle of the experiment. For spectroscopy near 10 000 cm⁻¹, molecules were first coherently transferred by STIRAP to $X(v = 73,$

$J = 2)$, and then irradiated with light near 1350 nm, as described in Ref. [12]. For detection, the molecules were transferred back to the original weakly bound state, dissociated, and the resulting atoms were imaged by absorption imaging. For STIRAP, the lasers were stabilized to reach both a short-term linewidth and long-term stability on the kHz level by locking to optical resonators and additional referencing to a stabilized optical frequency comb. However, wave-meter calibration was estimated to be 0.01 cm⁻¹, presenting a limitation on the absolute frequency accuracy of these transitions. Ultimately, the radiative linewidth of perhaps 1 MHz would limit the resolution.

Approximately 14 $A-b$ levels excited from X state levels near $v = 73$ are included in the data set analyzed in the present work. These term values are listed in Table I of [12] in connection with an earlier version of the present analysis.

D. Fluorescence from higher-lying states

These data were obtained at Tsinghua University, and are taken from Ref. [51]. Two successive diode lasers, each of 5 MHz linewidth, were used to excite $A^1\Sigma_u^+ \leftarrow X^1\Sigma_g^+$ and $2^3\Delta_{1g} \leftarrow A^1\Sigma_u^+$ transitions. Fluorescence from $2^3\Delta_{1g} \rightarrow b^3\Pi_{0u}$ was dispersed with a 0.85 m double grating Spex 1404 monochromator. The accuracy of the fluorescence lines was estimated to be about 1.5 cm⁻¹, with some better and others worse.

E. Data from OODR polarization spectroscopy, facilitated by collisional molecular orientation transfer

V-type optical-optical double-resonance (OODR) polarization spectroscopy was performed at Temple University to obtain data on mixed $A-b$ levels in a region of energy not studied previously. Among different types of polarization spectroscopy [54–57], this technique is well suited to observe selected transitions in the congested spectra of Cs₂ since in the single-laser based sub-Doppler experiments, the assignment of spectral lines is not trivial. Furthermore, collisional transfer of orientation produces a series of well-separated spectral lines associated with nearby levels that have been oriented and polarized. Another possible approach might be optical triple resonance, as used for Li₂ [36], Na₂ [40], and K₂ [44,45]. This approach would overcome the unfavorable Franck-Condon factors mentioned below, but would not yield the range of J values obtained in the present work, since optimization of signal to noise through cooling of the sample molecules would probably be necessary.

As in previous implementations of this technique (see [48] and [22], and references therein), a circularly polarized pump laser beam, tuned to a chosen transition, creates an anisotropic distribution of magnetic sublevel populations (net orientation) in one or more ground-state rovibrational levels. The counterpropagating linearly polarized probe laser beam can be considered to be made up of equal parts left- and right-circular polarization. When the probe frequency is tuned to a transition sharing either level with the pump transition, the orientation created by the pump causes the two circularly polarized probe components to experience different absorption coefficients (circular dichroism) and different indices of

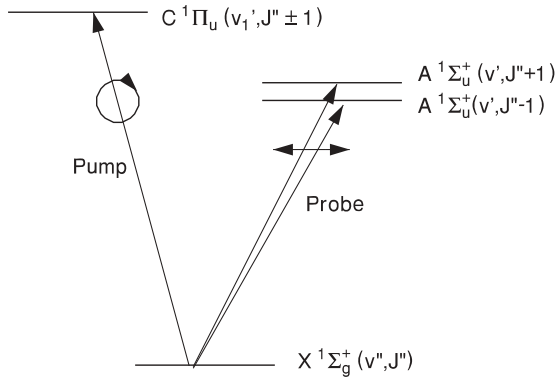


FIG. 1. A schematic of the transitions used for OODR polarization spectroscopy.

refraction (circular birefringence). Consequently, when the probe beam exits the oven, the two components no longer sum to the initial linear polarization, but rather the beam has a slight elliptical polarization and some fraction of it is transmitted through a final crossed linear polarizer before reaching the detector. Figure 1 shows schematically the transitions in this technique. (More information on the $C^1\Pi_u$ state is available from the potentials shown in Fig. 5.) A representation of the apparatus is shown in [22]. The experimental setup used here was similar to the one used previously for Rb_2 [48].

Collisional lines help to expand the data field but can only be observed if orientation is transferred from the ground-state level labeled by the pump laser to a neighboring level. A quantitative study of the transfer of population and orientation in collisions of NaK molecules with argon and potassium atoms has been carried out and reported in [58] and [59]. These references discuss the transfer of orientation following the discussion of Ref. [60], and also present a complete analysis of polarization spectroscopy line shapes, extending the textbook presentation in [61].

In our experiments, the Cs_2 metal was loaded at the center of a five-arm heat pipe oven, which was kept at a temperature of 550 K, with 3 Torr Argon buffer gas. A CR-699-29 tunable single mode laser with Kiton Red 620 dye was used as the circularly polarized pump laser, tuned to known [62] Cs_2 $C^1\Pi_u(v', J' = J'' \pm 1) \leftarrow X^1\Sigma_g^+(v'', J'')$ transitions. A CR-899-29 Ti:sapphire single-mode laser served as the linearly polarized probe laser. The two lasers were counterpropagating and overlapped in the center of the heat pipe with a crossing angle that was minimized so as to maximize the overlap area. The power of the pump (probe) laser was 100 mW (20 mW) in front of the heat pipe. The spot sizes (defined as a radius at $1/e^2$ intensity) of the pump (1.2 mm) and probe (0.9 mm) laser beams in the interaction region were measured with a razor-blade technique [64]. Two lenses were placed in the path of each laser beam for collimation inside the heat pipe.

A Glan Thompson linear polarizer and a $\lambda/4$ Babinet-Soleil compensator from Karl Lambrecht Corp. [63] were used to make the pump beam circularly polarized. Two linear polarizers in the probe laser beam path (one before and one after the heat-pipe oven) had relative transmission axes at a 90-degree angle for maximum extinction of the

probe laser when it was off resonance. A power meter (Coherent LabMax TO) with a sensitive detector (LM-2) placed after the second polarizer was used to make fine adjustments of the orientation of the second polarizer to create an optimal extinction ratio of 10^{-6} (and then removed for data acquisition). The observed ratio includes effects of window birefringence and circular dichroism. A photomultiplier tube (Hamamatsu R636-10) detected the polarization signal. Its output was amplified using a lock-in amplifier (Stanford Research Systems SR 850) for phase sensitive detection. The pump laser was modulated at a frequency of 980 Hz using a mechanical chopper (Stanford Research Systems SR 540).

The pump laser was calibrated using an iodine atlas [65,66], with estimated accuracy of $\sim 0.004 \text{ cm}^{-1}$. The Ti:sapphire laser was calibrated by comparing optogalvanic spectroscopy signals from a uranium lamp to line positions in the uranium atlas [67] when it scanned above $11\,000 \text{ cm}^{-1}$. The listed wave numbers in the uranium atlas are accurate to $\pm 0.003 \text{ cm}^{-1}$. A Burleigh 1600 wave meter and BOMEM DA8 FTIR were used to calibrate the Ti:sapphire frequency when it scanned below $11\,000 \text{ cm}^{-1}$. The calibrated wave numbers of the experimental peaks were added to the term values of their corresponding ground-state levels, calculated from the Dunham parameters of [50], to get the A - b state term values.

Because the Franck-Condon factors for transitions of interest were weaker by a factor of 100 in Cs_2 than for the Rb_2 lines in [48], the signal-to-noise ratio was smaller and fewer collisional satellites were observed than with Rb_2 ($\Delta J \leq 12$ rather than ≤ 58). Also, due to spectral congestion in Cs_2 , the pump transitions were difficult to isolate. Some of the pump transitions were confirmed by analyzing the resolved fluorescence recorded by a SPEX model 1404 dual grating 0.85 m monochromator. Other pump transitions were confirmed by scanning the pump laser while the probe laser was tuned to a previously assigned collisional peak.

26 different $C \leftarrow X$ transitions (ground state $3 \leq v \leq 8$ and $52 \leq J \leq 121$) were confirmed and 20 of them served as pump transitions in the experiment presented in this work. These transitions are listed in [52].

Figure 2 shows one OODR polarization spectroscopy data scan. For homonuclear molecules, the selection rule for collisions is $\Delta J = \text{even}$ due to the symmetry properties of the nuclear spin wave functions (for states that are not parity doubled). However, in the case shown in Fig. 2, the $C^1\Pi_u$ and $X^1\Sigma_g^+$ rotational spacings are such that two pump transitions $C^1\Pi_u(7,73) \leftarrow X^1\Sigma_g^+(6,74)$ and $C^1\Pi_u(7,72) \leftarrow X^1\Sigma_g^+(6,73)$ overlap within their Doppler widths and are therefore simultaneously excited. Thus Fig. 2 shows two separate collisional series (both characterized by $\Delta J = \text{even}$) starting from labeled ground-state levels (6,74) and (6,73). In this scan, the off-resonance baseline is artificially created by a nonzero offset added by the lock-in amplifier. The P -branch lines are positive-going relative to this offset, and the R -branch lines are negative-going here. The lock-in was used here in the “R” mode, in which the reported signal is the square root of the sum of the squares of the “in phase” and “in quadrature” components, and hence must always be positive.

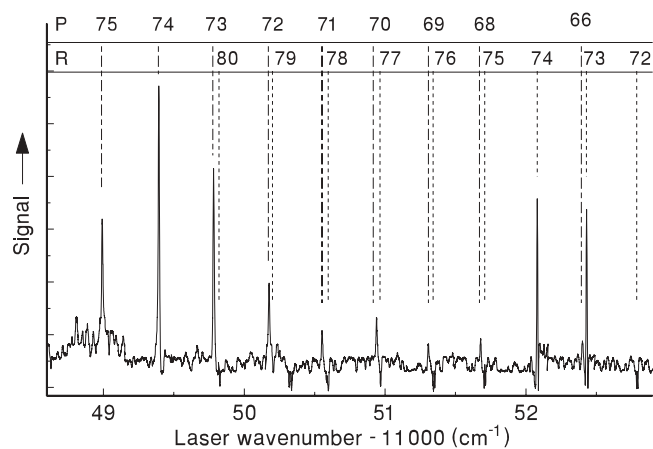


FIG. 2. OODR polarization spectroscopy signals. For this scan, the pump laser was set to $15\,898.5535\text{ cm}^{-1}$, simultaneously labeling the lower levels of the transitions $C^1\Pi_u(7,73)-X^1\Sigma_g^+(6,74)$ and $C^1\Pi_u(7,72)-X^1\Sigma_g^+(6,73)$. In this scan, P -branch lines are always positive going, and R -branch lines are negative going, except for the strong lines, $R(73)$ and $R(74)$, that reflect off the baseline as described in the text. Note that transitions from the $J = 74$ pumped level are relatively strongest. Those associated with other lower state rotational quantum numbers are due to collisional transfer of orientation.

Thus if the R -branch lines are particularly strong, they will reflect off the zero signal baseline, appearing as a central peak with minima on either side, as shown in Figs. 3(b) and 3(c). The fact that R -branch and P -branch lines have opposite signs (as always occurs if an offset is used or if only the “in phase” channel is recorded) is helpful for making assignments. In [48], the lock-in R mode was also used, but without an offset, so P and R lines both appeared positive going in the polarization scans reported in that work.

F. X -state term values

Recently Coxon and Hajigeorgiou [53] have reanalyzed the data of Amiot and Dulieu [50] on Cs_2 A - X transitions to make a direct fit to a potential of the $X^1\Sigma_g^+$ state, and hence to obtain improved X -state term values. It has come

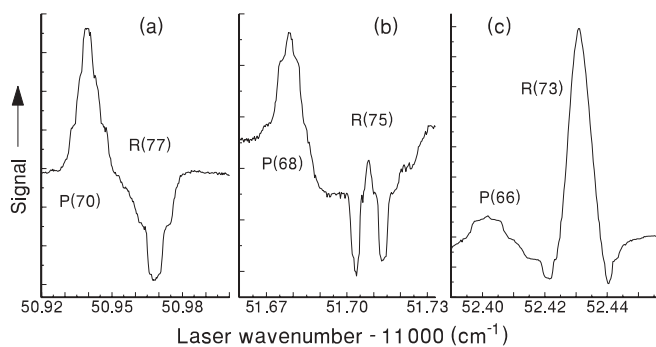


FIG. 3. OODR polarization spectroscopy line shapes for the particular conditions used in the present experiments. In each panel, there is a positive-going P line and an R line. In (a), the R line is weak and entirely negative going. In (b) and (c), the R line is stronger and reflects off the zero-signal baseline, producing a double minimum line shape. The vertical scale varies between (a)–(c), as can be seen by comparison with the previous figure.

to be recognized, as asserted in [68], that using a direct fit to an analytic potential is more precise than the semiclassical Dunham procedure. The differences in this case are less than 0.01 cm^{-1} , but nevertheless significant compared to residuals from least squares fits to A - b state term values presented below. Supplementary data associated with [53] give X -state term values for transitions in the data set of [50]. For other transitions used in this study, we have calculated X -state term values from the potential of [53]. In doing this, we have used the discrete variable representation (DVR) described below, to obtain eigenvalues of high- v and high- J levels without the use of high-order Dunham coefficients. When compared with X -state term values listed by [53], these values agreed to within $4 \times 10^{-4}\text{ cm}^{-1}$.

G. Summary of the data

Figure 4 summarizes the experimental data used in this study. It will be noted that the data from Temple University partially fill in a gap, and that (high-resolution) data from Tsinghua and Riga augment the data available near the minimum of the A state (as shown more clearly in Fig. 10). The various gaps in the data are associated with regions of low Franck-Condon factors (see Sec. V) and unavailability of lasers of suitable wavelength. Data from Innsbruck, at low- J values, extend up to $12\,600\text{ cm}^{-1}$ above the minimum of the X state. However, because data in this region were very limited, we were not able to extend the least squares fits to the

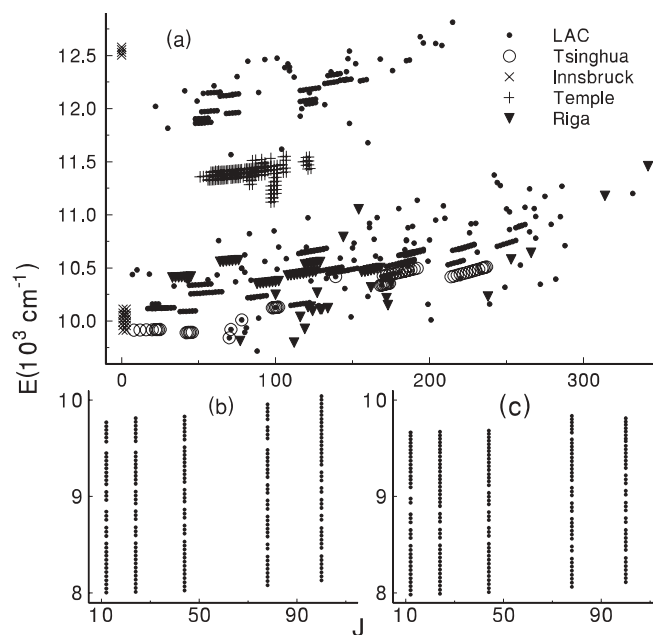


FIG. 4. Term value data used for this study. (a) Higher resolution FTS, OODR, and cold molecule spectroscopy term values. (b) and (c) display lower resolution (monochromator) data from Tsinghua University, on e and f parity levels, respectively. Energies in this plot are relative to the minimum of the $X^1\Sigma_g^+$ ground state. The Innsbruck data above $12\,500\text{ cm}^{-1}$ were actually not used in the fit. However, all other data shown here fall within the limit $E_{\text{red}} = E - 0.0091J(J+1) < 12\,400\text{ cm}^{-1}$, and are included in the least squares fit. (Please see Fig. 10 for a clearer picture of the extent of data near the minimum of the A state, for example.)

data beyond a reduced energy $E_{\text{red}} = E - 0.0091J(J+1)$ of $12\,400\text{ cm}^{-1}$.

When working with data from different sources, there is always a question of relative calibration errors. The average residuals (shown in Table I below) indicate that in this case differential calibration errors are smaller than the rms residuals from the fitting process. There were few cases of overlapping data to pose a more severe test for calibration differentials. Six term values measured by LAC and Tsinghua displayed an average difference of 0.0025 cm^{-1} .

III. ANALYSIS OF THE DATA

Because the data are relatively sparse in certain regions, the analysis requires special procedures and furthermore the quality of the fit is not quite comparable to that of Ref. [25], for example. Many of the methods are similar to those used in previous studies [25,48], and therefore will be summarized briefly, with attention to the special procedures mandated by the available data set. It is important to note also that for this relatively heavy alkali dimer, the second-order spin-orbit (SO2) effects become significant, and will require special attention below.

A. Hamiltonian elements

The molecular Hamiltonian [69]

$$H = H_{\text{BO}} + H_K + H_{\text{SO}} + H_{\text{rot}}, \quad (1)$$

includes the Born-Oppenheimer potentials H_{BO} , radial kinetic energy H_K , nuclear rotation H_{rot} , and spin-orbit interaction H_{SO} . Hyperfine structure has not yet been observed, but in Sec. VI, we attempt to estimate the magnitude of the hyperfine structure in the relevant states of Cs_2 .

The observed term values consist of levels of $b^3\Pi_{0u}^{\pm}$ below $v=0$ of the $A^1\Sigma_u^+$ state, together with many levels that can be identified as mixtures of $A^1\Sigma_u^+$ levels and $b^3\Pi_{0u}^+$ levels. In the first category are levels of both parity $(-1)^J$ (e symmetry) and parity $-(-1)^J$ (f symmetry). Overall, only a few levels were found to have significant $^3\Pi_1$ character and no levels with significant $^3\Pi_2$ character were identified. In view of the very limited information on the $^3\Pi_1$ levels, our $^3\Pi_0$ potential contains the spin-orbit function implicitly. When $^3\Pi_1$ and $^3\Pi_2$ levels are considered, the matrix elements of $H_{\text{BO}} + H_{\text{SO}} + H_{\text{rot}} + H_{\text{SO}_2}$ are [69]

$$\begin{aligned} \langle ^1\Sigma_u^+ | H | ^1\Sigma_u^+ \rangle &= U_A + (x+2)B + U_A^{\text{SO}_2}, \\ \langle ^3\Pi_{0u}^+ | H | ^3\Pi_{0u}^+ \rangle &= U_{b_0}^+ + (x+2)B + U_{b_{0e}}^{\text{SO}_2}, \\ \langle ^3\Pi_{0u}^- | H | ^3\Pi_{0u}^- \rangle &= U_{b_0}^- + (x+2)B + U_{b_{0f}}^{\text{SO}_2}, \\ \langle ^3\Pi_{1u} | H | ^3\Pi_{1u} \rangle &= U_{b_0}^+ + (x+2)B + \xi_{b_{10}}^{\text{SO}}, \\ \langle ^3\Pi_{2u} | H | ^3\Pi_{2u} \rangle &= U_{b_0}^+ + (x-2)B + \xi_{b_{10}}^{\text{SO}} + \xi_{b_{21}}^{\text{SO}}, \quad (2) \\ \langle ^1\Sigma_u^+ | H | ^3\Pi_{0u}^+ \rangle &= -\sqrt{2}\xi_{Ab_0}^{\text{SO}}, \\ \langle ^3\Pi_{0u} | H | ^3\Pi_{1u} \rangle &= -\sqrt{2x}B, \\ \langle ^3\Pi_{1u} | H | ^3\Pi_{2u} \rangle &= -\sqrt{2(x-2)}B, \\ \langle ^1\Sigma_u^+ | H | ^3\Pi_{1u} \rangle &= -\sqrt{2x}B\eta, \end{aligned}$$

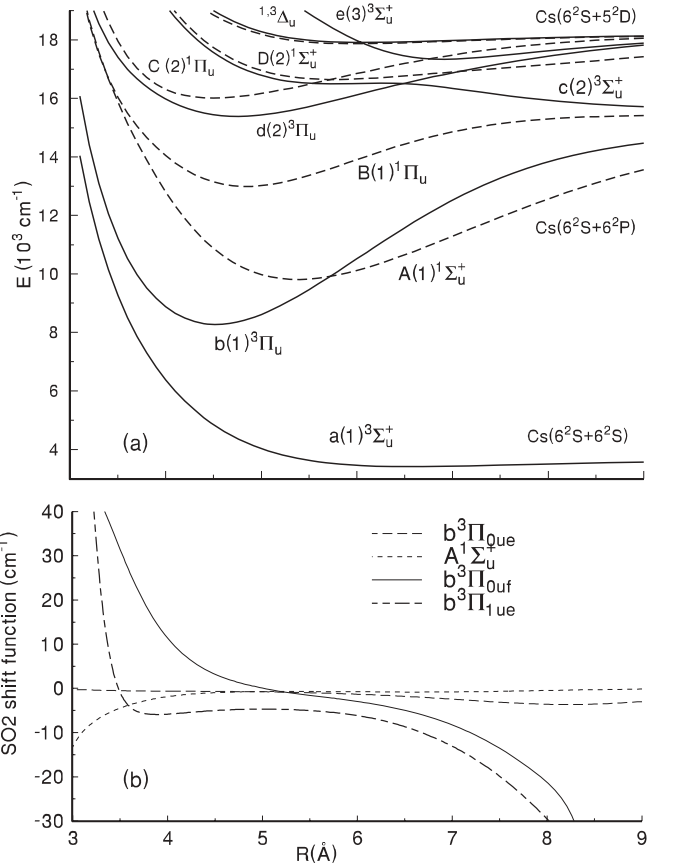


FIG. 5. (a) Potentials for *ungerade* states of Cs_2 dissociating to the three lowest atomic limits, as calculated from ECP-CPP-CI methods. (b) Second-order spin-orbit shifts for $A^1\Sigma_u^+$, $b^3\Pi_{0u}^{\pm}$, and $b^3\Pi_{1ue}$ calculated from these potential functions and the spin-orbit coupling functions, using Eqs. (3)–(6).

where $x = J(J+1)$, and $H^T = H$, where H^T is the transpose of H . In the above, the potentials, U_A and $U_{b_0}^{\pm}$, as well as the spin-orbit functions, $\xi_{Ab_0}^{\text{SO}}$ (off-diagonal) and $\xi_{b_{10}}^{\text{SO}}$, $\xi_{b_{21}}^{\text{SO}}$ (on-diagonal); and also $B \equiv \hbar^2/2\mu r^2$ are functions of internuclear distance r (μ is the reduced mass). $\xi_{b_{10}}^{\text{SO}}$ is the $\Omega = 1 - 0^+$ interval of the b state, and $\xi_{b_{21}}^{\text{SO}}$ is the $\Omega = 2 - 1$ interval. Both $\xi_{b_{10}}^{\text{SO}}$ and $\xi_{b_{21}}^{\text{SO}}$ functions include the SO2 effect implicitly. The parameter η arises from second-order spin-orbit and electronic-rotational effects, as discussed in [24].

The second-order spin-orbit (SO2) terms in the above Hamiltonian elements have been estimated by *ab initio* calculations using the present quasirelativistic ECP-CPP-CI procedures described in Sec. IV A. These functions are plotted in Fig. 5(b) and given numerically in [52]. The SO2 functions plotted in Fig. 5(b) are

$$U_A^{\text{SO}_2}(r) = \frac{2|\xi_{A-j}^{\text{SO}}|^2}{U_A - U_j}; \quad j \in (2)^3\Pi_u, \quad (3)$$

$$U_{b_{0e}}^{\text{SO}_2}(r) = \frac{2|\xi_{b_{0-j}}^{\text{SO}}|^2}{U_{b_0}^+ - U_j}; \quad j \in (2)^1\Sigma_u^+, \quad (4)$$

$$U_{b_{0f}}^{\text{SO}_2}(r) = \sum_j \frac{2|\xi_{b_{0-j}}^{\text{SO}}|^2}{U_{b_0}^- - U_j}; \quad j \in (1-3)^3\Sigma_u^+, \quad (5)$$

$$U_{b1e}^{SO2}(r) = \sum_j \frac{|\xi_{b1-j}^{SO}|^2}{U_{b1}^+ - U_j}; \quad j \in (1-3)^3\Sigma_u^+; (1-2)^1\Pi_u. \quad (6)$$

From Fig. 5(b), it is evident that U_{b0f}^{SO2} is large and positive for $r < 5.2 \text{ \AA}$, and becomes negative for large r . This behavior can be understood from the $b^3\Pi_{0u}^- - a^3\Sigma_u^+$ spin-orbit coupling function, which shifts the $b^3\Pi_{0u}^-$ energies upward at small r , because the $a^3\Sigma_u^+$ potential lies just below the $b^3\Pi_{0u}^-$ potential in this region. At larger values of r , the $b^3\Pi_{0u}^-$ potential approaches various *ungerade* potentials from below, as seen in Fig. 5(a), and thus the SO2 shift is negative

B. Analytic potential and spin-orbit forms

Although an ideal deperturbation analysis should yield the identical U_{b0}^+ and U_{b0}^- PECs (potential energy curves) for the triplet state, the experimental term values assigned to the $e(+)$ and $f(-)$ parity levels were involved in the fitting process separately. The empirical PECs of the interacting $A^1\Sigma_u^+$ and $b^3\Pi_{0u}^+$ diabatic states U_A , U_{b0}^+ were represented analytically by the expanded Morse oscillator (EMO) function [70,71]:

$$U(r) = T_e + D_e[1 - e^{-\alpha(r-r_e)}]^2; \quad (7)$$

$$\alpha(r) = \sum_{i=0}^N a_i \left(\frac{r^p - r_{\text{ref}}^p}{r^p + r_{\text{ref}}^p} \right)^i$$

converging to the appropriate dissociation limit, namely: $T^A = T_{\text{dis}} - D_e^A$ for the the singlet A state and $T_e^{b0} = T_{\text{dis}} - \xi_{Cs}^{SO} - D^{b0}$ for the $\Omega = 0$ substate of the triplet b state. Here $\xi_{Cs}^{SO} \equiv [E_{6^2P_{3/2}} - E_{6^2P_{1/2}}]/3 = 184.6796 \text{ cm}^{-1}$ is the empirical spin-orbit constant of the Cs atom in the 6^2P state [72] while $T_{\text{dis}} = D_e^X + E_{6^2P} - E_{6^2S}$ is the energy of the center of gravity of the Cs(6^2P) doublet (without hfs splitting) relative to the minimum of the X -state potential. From [72] $E_{6^2P} - E_{6^2S} = 11547.6275 \text{ cm}^{-1}$. The dissociation energy of the ground state (for the hfs center-of-gravity) $D_e^X = 3650.0299(14) \text{ cm}^{-1}$ from Ref. [11], taking into account a correction of -0.0022 cm^{-1} for the energies of $X(v = 71-73)$ levels, following [53]. Thus $T_{\text{dis}} = 15197.6574 \text{ cm}^{-1}$. Note that because of the U_A^{SO2} and U_{b0}^{SO2} terms, the effective potential minima differ from the fitted T_e values.

Both off-diagonal ξ_{Ab0}^{SO} and on-diagonal ξ_{b10}^{SO} , ξ_{b21}^{SO} empirical spin-orbit coupling functions were approximated by the Hulbert-Hirschfelder (HH) potential [73]

$$\xi^{SO}(r) = \xi_{Cs}^{SO} - D_e^{SO}[2e^{-x} - e^{-2x}[1 + cx^3(1 + bx)]]; \quad (8)$$

$$x = a(r/r_e^{SO} - 1)$$

determined by the five fitted parameters D_e^{SO} , r_e^{SO} , a , b , and c .

The initial EMO and HH parameters of the relevant PECs and SO functions were estimated using the present quasirelativistic ECP-CPP-CI electronic structure calculation. The refined parameters of the PECs and SO coupling functions ξ_{Ab0}^{SO} and ξ_{b10}^{SO} were determined iteratively using a weighted nonlinear least-square fitting (NLSF) procedure. As there were no data on $b^3\Pi_{2u}$, the initial *ab initio* estimate for ξ_{b21}^{SO} was used in the least squares fits.

C. Fitting procedures

The spin-orbit coupling function between the $A^1\Sigma_u^+$ and $b^3\Pi_{0u}^+$ states of Cs_2 is larger than the vibrational intervals, thus requiring careful treatment of perturbative interactions. Initially, the least squares fitting was performed with a 2×2 Hamiltonian matrix, including simply the $\Omega = 0^+$ manifolds and the off-diagonal spin-orbit coupling term, ξ_{Ab0}^{SO} . The two-channel fit was crucial in determining nearly final potentials. The details of the robust fitting procedure used are given elsewhere [24,25]. Next a 3×3 Hamiltonian included $^3\Pi_1$ levels and ξ_{b10}^{SO} . Final fits were made with a four-channel Hamiltonian and ξ_{b21}^{SO} . Although $^3\Pi_2$ components were not directly observed, they affected the fitted parameters through the terms coupling with $^3\Pi_1$ and thus indirectly to $^3\Pi_0^+$. These multichannel calculations utilized both finite-difference (FD) and discrete variable representation (DVR) approaches. For additional details on the FD and DVR numerical methods, please see [24] and [48], respectively. It was determined that if identical potential and spin-orbit functions are used, the eigenvalues obtained from the FD and DVR methods are in excellent agreement.

D. Fitted parameters, potentials, spin-orbit functions, and term values

The e -parity term value data was fit with 12(8) potential parameters, a_i in Eq. (7), for the $b^3\Pi_{0u}^+(A^1\Sigma_u^+)$ state, plus r_e and T_e for each state. The HH forms [Eq. (8)] used for ξ_{Ab0}^{SO} and ξ_{b10}^{SO} required five fit parameters each, while the parameters for ξ_{b21}^{SO} were provided by *ab initio* calculations (ECP1). The range of the fitted data extended from 7982 cm^{-1} ($v = 0$, $J = 12$ of $b^3\Pi_{0u+}$) to 12812 cm^{-1} , $J = 326$. But a more meaningful measure is the reduced energy, $E_{\text{res}} = E - 0.0091J(J+1)$, which extended only to 12390 cm^{-1} . By contrast, the dissociation limits of the $b^3\Pi_{0u}$ and $A^1\Sigma_u^+$ states lie at 15012.98 cm^{-1} and 15197.66 cm^{-1} , respectively. The SO2 shift terms, calculated by Eqs. (3), (4), (5) and given numerically in [52], were added to the $A^1\Sigma_u^+$ and $b^3\Pi_{0u}^\pm$ potentials.

Because of the relatively large uncertainty in the SO2 terms, data for $b^3\Pi_{0u}^-$ (f parity) were not included in the fit.

The quality of the final fit to the e -parity data is indicated by the plotted residuals in Fig. 6, and displayed for the individual data sets in Table I. Table II gives the fitted potential parameters together with results from *ab initio* ECP-CPP-CI calculations. Table III gives parameters for the empirical off-diagonal and diagonal spin-orbit functions. Figure 7 displays the empirical potentials for the $A^1\Sigma_u^+$ and $b^3\Pi_{0u}^+$ states over the range of the data, namely up to 12400 cm^{-1} above the minimum of the X state.

Numerical values for the potentials and spin-orbit functions, parameter listings, calculated term values, and comparisons between calculated and observed term values, and several plots of calculated and observed term values are all given in [52].

It should be noted that in fitting the data for $+(e)$ -parity levels from the Tsinghua monochromator (low-resolution) data, it was found that assigning certain terms to $^3\Pi_{2u}$ rather than $^3\Pi_{0u}^+$ reduced the residuals. Ultimately, such assignments were not accepted because they violate known selection rules for pure Hund's coupling case (a). The larger residuals

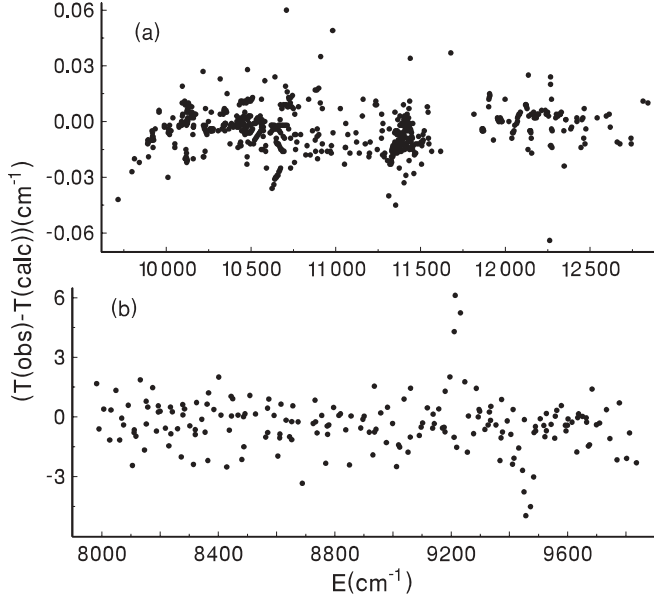


FIG. 6. Residuals from least squares fits. (a) shows residuals from fits to the high-resolution data from all four sources; (b) shows residuals from the fits to low-resolution (monochromator) data.

obtained when these levels were assigned to ${}^3\Pi_{0u}^+$ may be associated with the low intensities of some of the lines as noted in Ref. [51], or they may be associated with breakdown of Hund's case (a) selection rules due to spin-orbit effects.

The off-diagonal spin-orbit function ξ_{Ab0}^{SO} connecting $A^1\Sigma_u^+$ and $b^3\Pi_{0u}^+$ states is determined empirically from the perturbation crossings. The fitted parameters are given in Table III, and the fitted function is plotted in Fig. 8, together with *ab initio* functions for which the computational methods are discussed below. The fitted ξ_{Ab0}^{SO} function is primarily determined by its value at the potential crossing point, denoted r_x in this figure. It is satisfying that at r_x , the fitted function is indeed close to all three *ab initio* functions plotted also in this figure. For other values of r , there are significant differences.

The fine structure splitting between the $b^3\Pi_0$ and $b^3\Pi_1$ potentials could be deduced from the presently available data only from a few regions of avoided crossings in the rotational

TABLE I. Residuals from the least squares fit to Cs_2 A - b state data. N_p is the number of data points. Rms. denotes the root mean square residuals in cm^{-1} ; Ave. denotes the average residual (observed minus calculated term value), also in cm^{-1} . Tsinghua (LR) denotes the low-resolution (monochromator) data from Tsinghua University [51]: only e -parity levels were included in this fit. The experimental errors are approximately 1.5 cm^{-1} for Tsinghua (LR) and 0.01 cm^{-1} for the other data sets.

Source	N_p	Rms. (cm^{-1})	Ave. (cm^{-1})
LAC [50,53]	340	0.0154	0.0072
LAC [49]	55	0.0198	-0.0045
Tsinghua	58	0.0086	0.0028
Innsbruck	14	0.0075	0.0010
Temple	161	0.0114	-0.0006
Riga	75	0.0098	0.0041
Tsinghua (LR)(e)	194	1.554	-0.437

TABLE II. Parameters obtained from a fit to EMO potentials using Eq. (7), together with *ab initio* results. In each case, $r_{\text{ref}} = 5.0 \text{ \AA}$ and $p = 3$. r_e values are in \AA . T_e , $D_e = T_{\text{dis}} - T_e$, and ω_e are in cm^{-1} , and the other parameters are dimensionless. $\eta = -0.08228330$ is defined in Eq. (2). *Ab initio* ECP1-CPP-CI values for $b^3\Pi_{0u}$ are obtained from calculated $U({}^3\Pi_1) - \xi_{b10}^{SO}$. The ω_e values are obtained from the second derivative of the potentials at $r = r_e$.

	Expt.		<i>ab initio</i>	
	$b^3\Pi_{0u}^+$	$A^1\Sigma_u^+$	$b^3\Pi_{0u}^\pm$	$A^1\Sigma_u^+$
r_e	4.45746	5.32913	4.5031	5.3799
T_e	7977.8479	9587.1155	8077.8	9809.8
a_0	0.522 835 586	0.433 295 2472		
a_1	0.135 607 457	0.043 153 7069		
a_2	0.166 158 407	-0.018 277 337 44		
a_3	-0.097 477 983	0.120 617 659 70		
a_4	-0.521 843 942	-0.094 559 758 27		
a_5	1.904 713 4070	0.085 988 743 46		
a_6	1.737 199 081	0.426 592 638 34		
a_7	-7.992 154 379	-0.474 463 872 17		
a_8	0.076 434 068			
a_9	8.921 002 546			
a_{10}	-3.390 109 463			
D_e	7035.1427	5610.5398		
ω_e	42.6524	33.0055	43.133	31.953

progressions. We have found four such cases, three of which are shown in Fig. 9. From these deviations in the rotational level energies, we have fit the parameters (see Table III) that characterize the fine structure interval. The fitted ξ_{b10}^{SO} function and an *ab initio* result are plotted in Fig. 8. The minimum of this empirical fine-structure splitting function is approximately 139 cm^{-1} , as compared with the minima of the analogous functions for RbCs and KCs, reported to be 71.4 cm^{-1} [27] and 78.26 cm^{-1} [25], respectively, both based on more complete $b^3\Pi_1$ data than are presently available for Cs_2 . The ECP-CPP-CI *ab initio* spin-orbit functions happen to be in good agreement with the empirical function. It should be noted that fits of comparable quality were obtained with an empirical ξ_{b10}^{SO} function exhibiting a minimum of $\approx 120 \text{ cm}^{-1}$, hence with a different vibrational numbering for the $b^3\Pi_{1u}$ manifold. The preference for the function plotted in Fig. 8 was based on close agreement with *ab initio* results, in view of the good agreement between empirical and *ab initio* SO functions in the case of KCs [25].

TABLE III. Parameters for the spin-orbit functions in the Hulbert-Hirschfelder form given in Eq. (8). The parameters for ξ_{Ab0}^{SO} and ξ_{b10}^{SO} are from the least squares fit, while those for ξ_{b21}^{SO} are from *ab initio* calculations. In each case, $\xi_{Cs}^{SO} = 184.6796 \text{ cm}^{-1}$. D_e^{SO} values are in cm^{-1} , r_e^{SO} are in \AA , and a, b , and c are dimensionless.

	ξ_{Ab0}^{SO}	ξ_{b10}^{SO}	ξ_{b21}^{SO}
D_e^{SO}	70.870 86	46.101 16	37.2907
r_e^{SO}	5.968 745	6.288 671	6.341 088
a	2.252 68	3.342 71	3.132 78
b	1.221 883	0.473 373	0.421 783
c	0.325 679	0.405 0794	0.302 7172

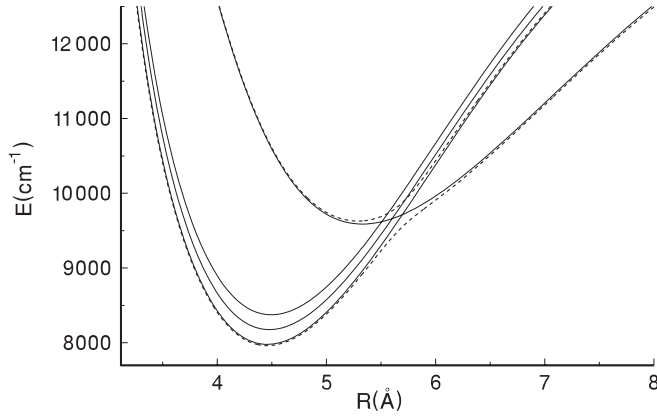


FIG. 7. Potentials for the Cs_2 $A^1\Sigma_u^+$ and $b^3\Pi_u$ states obtained from fits to the data in this work, over the range sampled by the data. The $b^3\Pi_{2u}$ potential (uppermost of the set of three) is obtained from *ab initio* calculations only. The dashed lines indicate the adiabatic 0_u^+ potentials, obtained by diagonalizing the diabatic A and $b0$ potentials with the spin-orbit coupling term, ξ_{Ab0}^{SO} .

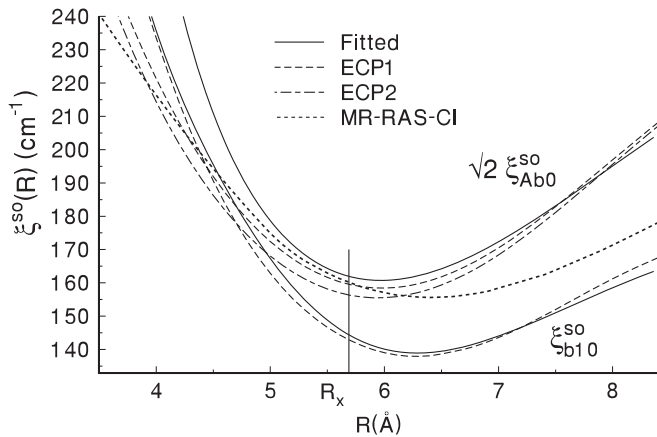


FIG. 8. Fitted and *ab initio* off-diagonal spin-orbit function, $\sqrt{2}\xi_{Ab0}^{\text{SO}}$, coupling the $A^1\Sigma_u^+$ and $b^3\Pi_{0u}^+$ states, together with the diagonal function, ξ_{b10}^{SO} , that gives the fine-structure splitting between $b^3\Pi_u^+$ and $b^3\Pi_{0u}^+$. Both MR-RAS-CI and ECP-CPP-CI procedures were used for the *ab initio* functions, as indicated. For the latter, the upper (lower) line represents results from ECP1 (ECP2) basis sets. The vertical line denotes the value $r = r_x$ of the potential crossing point. For ξ_{b10}^{SO} , the ECP1 and ECP2 results agreed to within the linewidth.

TABLE IV. Parameters fit to adiabatic 0_u^+ potentials from various sources. Near r_e , the lower adiabatic potential is close to the $b^3\Pi_{0u}^+$ potential, while the upper adiabatic potential is close to the $A^1\Sigma_u^+$ potential. T_e and ω_e are in cm^{-1} , while r_e is in \AA .

	Expt.	ECP1-CPP-CI	Spies
T_e (lower)	7960.45	8064.79	8169.57
r_e (lower)	4.4583	4.5049	4.5028
ω_e (lower)	42.432	42.904	43.082
T_e (upper)	9626.64	9843.53	9598.16
r_e (upper)	5.2903	5.3465	5.3327
ω_e (upper)	36.541	34.066	35.135

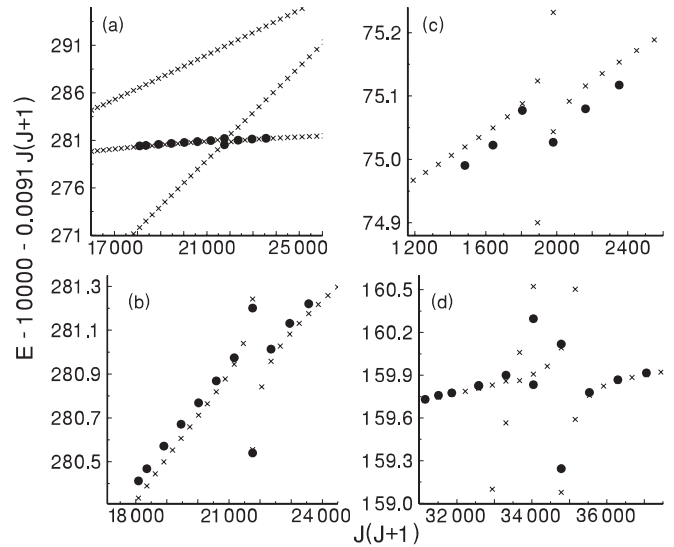


FIG. 9. Examples of avoided crossings between $\Omega = 1$ and $\Omega = 0^+$ levels. (a) shows the relatively steeper slope of $\Omega = 1$ levels in a plot of reduced energy vs. $J(J+1)$. (b) is an enlargement of the crossing region in (a). (c) shows another crossing region. In (d), a crossing between mixed $\Omega = 0^+$ levels lies very near to an $\Omega = 1$ level. Small \times s denote calculated term values, larger filled circles are observed term values in these plots.

The last two columns of Table II give *ab initio* ECP1-CPP-CI results for parameters derived from $U(A^1\Sigma_u^+)$ and from $U(b^3\Pi_{0u}^+) - \xi_{b10}^{\text{SO}}$. It is also interesting to compare results from our least squares fit to the experimental data with earlier calculations by Spies [74], which were not published but were widely circulated among people working with Cs_2 . However, since these calculations were primarily relativistic, they pertain to the adiabatic potentials, as shown by the dashed lines in Fig. 7. To make a comparison, we have calculated adiabatic potentials from the experimental potentials and from the *ab initio* ECP1-CPP-CI potentials (by diagonalizing the potentials plus appropriate spin-orbit functions as a function of r), and then we have extracted values for T_e , r_e , and ω_e , to compare with similar quantities fit to the potentials of Ref. [74]. Table IV shows that, considering the inherent limitations of quantum chemistry calculations, the earlier *ab initio* results were in moderately good agreement with current experimental results and *ab initio* results.

E. Energy-level structure

1. e-parity levels

Figure 10 displays term values calculated from fitted parameters together with the input term value data, on a reduced energy scale to flatten the rotational structure. One point to note here is that the experimental data for low levels of the A state are quite sparse as compared with the study of the A - b states of Rb_2 [48], for which it was possible to observe long rotational progressions that facilitated accurate fitted parameters. The top part of Fig. 10 displays a region with more ample data. Note that, despite the strong perturbative coupling, the effective rotational structure clearly differentiates states that are primarily $A^1\Sigma_u^+$, which have the

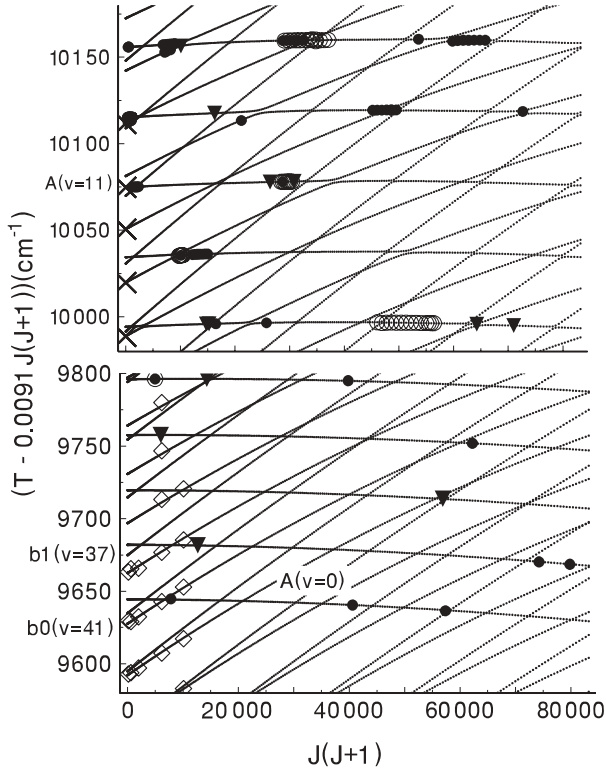


FIG. 10. Term values near $A(v) = 0$ (bottom), showing sparsity of data, and at higher energies (top), showing somewhat more abundant data from various sources. Open diamonds indicate monochromator data, open circles denote high resolution data, also from Tsinghua, closed circles denote high resolution data from LAC, X's denote data from cold molecule spectroscopy from Innsbruck, and triangles denote data from Riga. The most steeply sloping eigenvalues are for $\Omega = 1$ levels, the least steeply sloping are for levels that are primarily $A^1\Sigma_u^+$ in character.

least slope, from those that are primarily $b^3\Pi_{0u}^+$, which have a slope intermediate between the former and the $b^3\Pi_{1u}$ states. In this regard, please note in the top part of Fig. 10, that several of the levels observed in Innsbruck University by excitation from cold molecules in levels of the $X^1\Sigma_g^+$ state, appear to have primarily triplet character. This feature will be discussed further in Sec. V in connection with transition amplitudes between mixed A - b levels and X -state levels.

The contrast in rotational structure [slope vs. $J(J + 1)$] of A - b state levels seen in Fig. 10 persists up to approximately $v = 40$ of the A state. Higher levels, such as those shown in Fig. 11 exhibit a large degree of mixing such that it becomes impossible to assign vibrational quantum numbers.

2. f -parity levels: Origin of the $e - f$ Λ -doubling effect in the $b^3\Pi_{0u}$ substate

As was mentioned above the main contribution to the $\Omega(\Lambda)$ splitting of the $b^3\Pi_{0u}$ substate

$$\Delta_{fe} = E_{vJ}^f - E_{vJ}^e \quad (9)$$

comes from the strong spin-orbit coupling with the nearby singlet $A^1\Sigma_u^+$ state, the SO contribution. However, a significant contribution (SO2) comes also from the second-order spin-orbit shifts, which are written in Eq. (5), and plotted

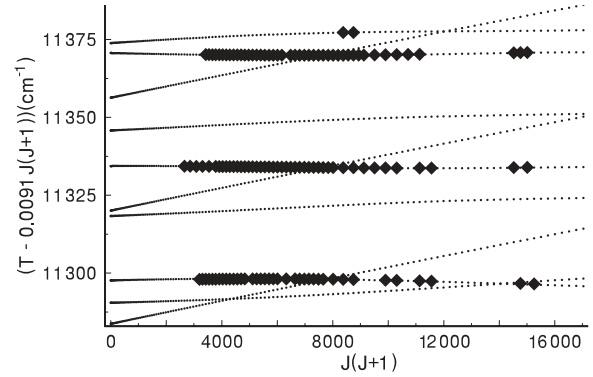


FIG. 11. Some of the term values (diamonds) measured at Temple University to partially fill a gap in earlier data. Smaller filled circles denoted calculated term values. Note that in this energy region, the 0_u^+ energy levels repel each other and do not exhibit narrow avoided crossings, as they do in the previous figure.

in Fig. 5(b). Theoretical values for the SO contribution are obtained by taking the difference between eigenvalues calculated with the fitted potentials with and without the off-diagonal ξ_{Ab0}^{SO} coupling function. Calculated values for the SO2 contributions are obtained as expectation values from the second-order perturbation shift functions, U_{b0e}^{SO2} and U_{b0f}^{SO2} , shown in Fig. 5(b), and the rovibrational wave functions calculated from the U_{b0}^- potential. The results are plotted in Fig. 12. There is a rapid rise as the $b^3\Pi_{0u}$ levels approach $A(v = 0)$. The contribution of SO2 terms increase more slowly between 3.5 and 5 cm^{-1} , as the $b^3\Pi_{0u}^-$ functions sample the SO2 shift function shown in Fig. 5(b). Because the SO2 terms are likely to be uncertain by 5–10% (hence possibly as much as 0.5 cm^{-1}), we have not attempted an empirical fit to the f parity data. There may also be an “intrinsic” e - f energy

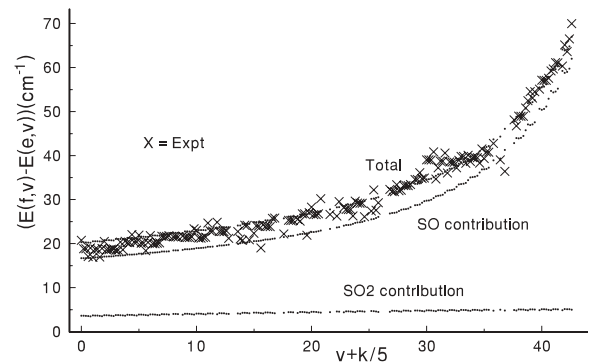


FIG. 12. Energy difference between e - and f -parity states for levels of $b^3\Pi_{0u}$, as a function of vibrational level, v , and rotational level. Results are plotted for the five values of J observed in [51], namely $J = 12, 24, 44, 78,$ and 100 . These J values are translated into $k = 0 - 4$, and the horizontal axis is $v + k/5$, so as to spread out the data on different- J levels. The theoretical SO2 contribution is obtained from the second-order spin-orbit coupling functions and the potential energy differences shown in Fig. 5. The theoretical SO contribution is the difference between the calculated energy with and without ξ_{Ab0}^{SO} . “Total” denotes the sum of the SO and the SO2 terms. Dots denote theoretical values, \times symbols denote experimental values.

difference due to spin-spin interaction terms, but we have not attempted to estimate such effects.

IV. *AB INITIO* CALCULATIONS OF POTENTIALS AND SPIN-ORBIT FUNCTIONS

In this section we discuss the methods used for *ab initio* calculations at Moscow State University and at Temple University.

A. Quasirelativistic ECP-CPP-CI calculations (at Moscow State University)

The potential energy curves, transition dipole moments, spin-orbit, and angular coupling matrix elements between the Cs₂ electronic states converging to the lowest three dissociation limits were evaluated in the basis of the spin-averaged wave functions corresponding to pure Hund's coupling case (a). The quasirelativistic matrix elements have been obtained for a wide range of internuclear distance by using effective core pseudopotential (ECP) [75]. The core-valence correlation has been taken in account using a large scale multireference configuration interaction (MR-CI) method [76] combined with semiempirical core polarization potential (CPP) [77]. All calculations were performed by means of the MOLPRO v.2008 program package [78].

To include relativistic effects, the inner core shell of the Cs atom has been replaced by spin-orbit averaged nonempirical small core nine-electron ECP, leaving 18 outer-core and valence electrons of the cesium dimer for explicit correlation treatment. In order to test the ECP basis set dependence of the present quasirelativistic calculations, completely different shape (ECP1) [79] and energy (ECP2) [80] consistent basis sets available for the Cs atom have been used. The original spin-averaged Gaussian basis sets from Refs. [79,80] were extended by additional diffuse and polarization functions while the relevant spin-orbit Gaussian sets were directly borrowed from the above references.

The molecular orbitals (MOs) of Cs₂ derived by the self-consistent field (SCF) method in the *D*_{2h} point group symmetry were then optimized by the solution of the state-averaged complete active space SCF (SA-CAS-SCF) problem for the lowest (1-5)^{1,3}Σ_{u,g}⁺, (1-3)^{1,3}Π_{u,g}, and (1)^{1,3}Δ_{u,g} states taken with equal weights [81]. The dynamical correlation effects were introduced by the internally contracted multireference configuration interaction method (MR-CI) [76]. The respective CAS consisted of the 7σ_{u,g}, 4π_{u,g}, and 2δ_{u,g} optimized MOs. MR-CI was applied for only two valence electrons keeping the rest frozen, i.e., in a full two-valence electron CI scheme while the *l*-independent core-polarization potentials (CPPs) with properly adjusted cutoff radii were employed to take into account the remaining core-polarization effects implicitly. The relevant spin-orbit Gaussian basis set coefficients were scaled in order to reproduce the experimental fine-structure splitting of the lowest excited Cs(6²P) state [72].

To elucidate the impact of the electron correlation effect on the present results, the CPP-CI energies and wave functions have been repeatedly evaluated by means of the lower *C*_{2v} group symmetry. In this case the respective CAS was restricted by the 14σ and 10π optimized MOs. The results obtained

in both *D*_{2h} and *C*_{2v} representations are found to be almost identical. Furthermore, the energies and matrix elements obtained in the framework of the same CPP-CI procedure by using ECP1 and ECP2 basis sets coincided with each other to within a few percent.

The resulting PECs for all electronic states of *u*-symmetry converging to the first-, second-, and third-dissociation limits are depicted in Fig. 5(a), while some of the relevant diagonal and off-diagonal spin-orbit coupling functions are compared in Fig. 8.

B. Multireference restricted active space configuration interaction (MR-RAS-CI) calculations (Temple University)

At Temple University, we have performed nonrelativistic as well as a relativistic electronic structure calculation to determine the strength of the spin-orbit coupling between the *A* ¹Σ_u⁺ and *b* ³Π_u potentials of Cs₂. One electron occupied orbitals are obtained from an atomic Hartree-Fock or Dirac-Fock calculation, respectively. Virtual, highly-excited orbitals are Sturm-type functions. The orbitals are labeled 1*s*, 2*s*, 2*p*, . . . , etc., in analogy with the principal quantum number and orbital angular momentum of the hydrogen atom. A configuration interaction based on molecular determinants selected by a multireference restricted active space (MR-RAS-CI) method is used [82]. Details on the implementation of this method in our calculations of heavy diatomic molecules are given in Ref. [83]. Finally, for the nonrelativistic CI calculation we have evaluated matrix elements of the spin-orbit operator

$$\hat{H}_{\text{SO}} = \frac{\alpha^2}{2} \sum_N \sum_i \frac{Z_N}{r_{iN}^3} \vec{l}_i \cdot \vec{s}_i - \frac{\alpha^2}{2} \sum_{i \neq j} \frac{1}{r_{ij}^3} [\vec{r}_{ij} \times \vec{p}_i] \cdot (\vec{s}_i + 2\vec{s}_j), \quad (10)$$

where α is the fine structure constant and \vec{s}_i is the spin of electron *i*. The first term of Eq. (10) is a one-electron operator that describes spin-orbit interactions between one nucleus and one electron. Here *r*_{*iN*} is the separation between the *i*th electron and nucleus *N* with charge *Z*_{*N*} and \vec{l}_i is the electron orbital angular momentum relative to nucleus *N*. The second term of Eq. (10) is a two-electron operator describing the spin-orbit interaction between electrons. Here \vec{r}_{ij} is the separation between electrons *i* and *j* and \vec{p}_i is the momentum of electron *i*.

The closed or filled orbitals up to the 4*d* shell of Cs form the core orbitals of the molecular determinants used in the CI for both the nonrelativistic and relativistic calculation. No excitations are allowed from these shells. The 5*s*² and 5*p*⁶ shells are core-valence orbitals and are in the active space from which single and double excitations are allowed. The 6*s* and 6*p* orbitals are also added to the active space and single, double, and triple occupancy is allowed. Finally, we use four each of the *s*, *p*, *d*, and *f* virtual Sturm orbitals to complete the active space. Up to double occupancy is allowed for these virtual orbitals.

The off-diagonal spin-orbit matrix elements of the nonrelativistic calculation is shown in Fig. 8. We find that the one-electron spin-orbit operator of Eq. (10) provides ~99% of the total value of the spin-orbit coupling.

The relativistic potential calculations give an avoided crossing between A - b potentials. The smallest energy difference ΔE is evaluated at $r = 5.5 \text{ \AA}$ and equals 326 cm^{-1} . According to degenerate perturbation theory, half of this value is equal to the off-diagonal ξ_{Ab0}^{SO} spin-orbit function at the same internuclear distance. Comparison of ξ_{Ab0}^{SO} at $r = 5.5 \text{ \AA}$ obtained by nonrelativistic and relativistic calculations shows a good agreement. To be precise, $\xi_{Ab0}^{SO}(5.5 \text{ \AA}) = 163.0, 161.6, 158.2,$ and 164.4 cm^{-1} , from MR-RAS-CI, ECP1, ECP2, and experiment, respectively.

V. TRANSITION AMPLITUDES TO X -STATE LEVELS

The distribution of intensities for transitions from or to the $X^1\Sigma_g^+$ state is important in testing model potentials and wave functions, for designing data acquisition procedures, and is also important for designing transition sequences to produce cold Cs_2 molecules from cold Cs atoms or from Cs Feshbach resonance states. Transition intensities can be evaluated by using nonadiabatic wave functions of the A - b complex calculated by FD or by DVR methods, and this section will present examples of each.

A. Radiative properties of the A - b complex

To test the reliability of the deperturbation analysis described above, we have evaluated the A - $b \rightarrow X$ transition probabilities, I , and radiative lifetimes τ of the A - b complex according to the relations

$$I_{A-b \rightarrow X} \propto v_{A-b \rightarrow X}^4 |\langle \phi_A | d_{AX} | v_X \rangle|^2, \quad (11)$$

$$\frac{1}{\tau_{A-b}} = \frac{8\pi^2}{2\hbar c} \sum_{v_X} v_{A-b \rightarrow X}^3 |\langle \phi_A | d_{AX} | v_X \rangle|^2,$$

where $v_{A-b \rightarrow X} = E^{\text{calc}}(J') - E_X(v_X; J_X)$ is the wave number of the rovibronic $A^1\Sigma_u^+ \sim b^3\Pi_u^+ \rightarrow X^1\Sigma_g^+$ transition. $d_{AX}(r)$ is the *ab initio* spin-allowed $A^1\Sigma_u^+ - X^1\Sigma_g^+$ transition dipole moment calculated in the present work by the ECP-CPP-CI method. $E^{\text{calc}}(J')$ is the energy and $|\phi_A\rangle$ is the nonadiabatic wave function of the A -state component which were obtained by the FD method from numerical solution of close coupled radial equations with the present empirical PECs and SO functions. The rovibronic eigenvalues E_X and eigenfunctions of the $X^1\Sigma_g^+$ state were obtained by solving the single channel radial equation using the empirical potential from [53].

The Riga group obtained FTS LIF fluorescence intensities over a range of X -state vibrational levels from a $J' = 238$ level with predominantly (calculated to be 88%) $v_A = 2$ character. Figure 13 shows the two predominant wave-function components of this state together with results of two computational methods for the *ab initio* transition dipole moment. The inset shows this moment over an extended range of r . The relative fluorescence intensities in Fig. 14 show good agreement between observed and calculated values.

The $\tau_{A-b} = 26 \text{ \mu s}$ value predicted for the metastable ground $v_b = 0$ level of the $b^3\Pi_{0u}^+$ state, which has only 0.5% admixture of the singlet A state, is very close to the experimental decay rate $\leq 5 \times 10^4 \text{ s}^{-1}$ measured by time-resolved fluorescence spectra of Cs_2 dimer molecules

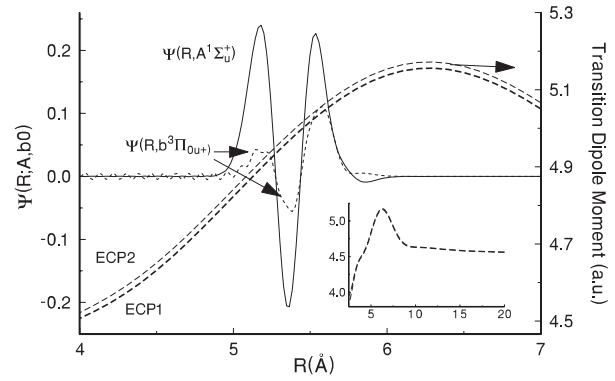


FIG. 13. (Left axis) Wave function components for an excited state level of $J = 238$, which consists mostly of $A^1\Sigma_u^+(v = 2)$, but also with a $b^3\Pi_{0u}^+$ component that is shown with dashed lines, indicated by two arrows. (right axis) Calculated transition dipole moment between the $A^1\Sigma_u^+$ and $X^1\Sigma_g^+$ state, in a.u. The ECP1 and ECP2 results from the ECP-CPP-CI method are shown as discussed in the text. The inset shows theoretical predictions for the transition dipole moment out to larger values of r .

immersed in a solid helium matrix [84]. The $\tau_{A-b} = 0.5 \text{ \mu s}$ obtained for the excited $v_b = 37$ level, which has 25% fraction of $A^1\Sigma_u^+$ character, can be compared with the experimental decay probability of $2.5 \times 10^3 \text{ s}^{-1}$ of the $b^3\Pi_u \rightarrow X^1\Sigma_g^+$ transition estimated from the kinetics of Cs_2 fluorescence measured as a function of temperature and Xe buffer gas density in [85].

B. Transition intensities

It was noted that the intensities for OODR polarization spectroscopy experiments at Temple University were much weaker than for analogous experiments with Rb_2 . An explanation for this was obtained from Franck-Condon (FC) factors, which showed that over the spectral region of interest here, the FC factors were about 100 times smaller than the FC factors that pertained to the observations of Rb_2 A - $b \leftarrow X$ transitions reported in [48]. A plot of FC factors to A - b levels of interest from X -state levels with $v \leq 6$ is shown in Fig. 15, for $J = 50$.

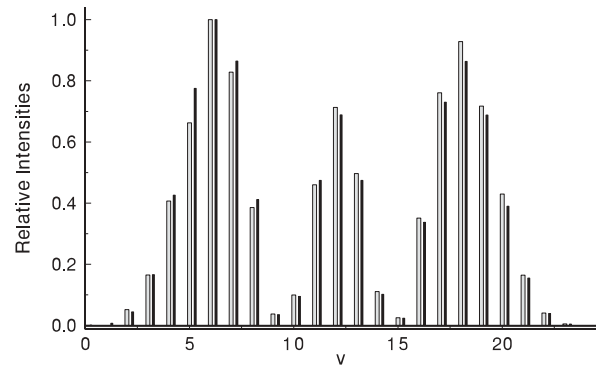


FIG. 14. Relative intensities for the fluorescence of the $J' = 238$ excited state, whose wave function components are shown in the previous figure, to vibrational levels of the $X^1\Sigma_g^+$ state, as measured in Riga (wider, open bars) and as calculated by the FD method (narrower, filled bars). Intensities are normalized to a maximum value of unity in each case.

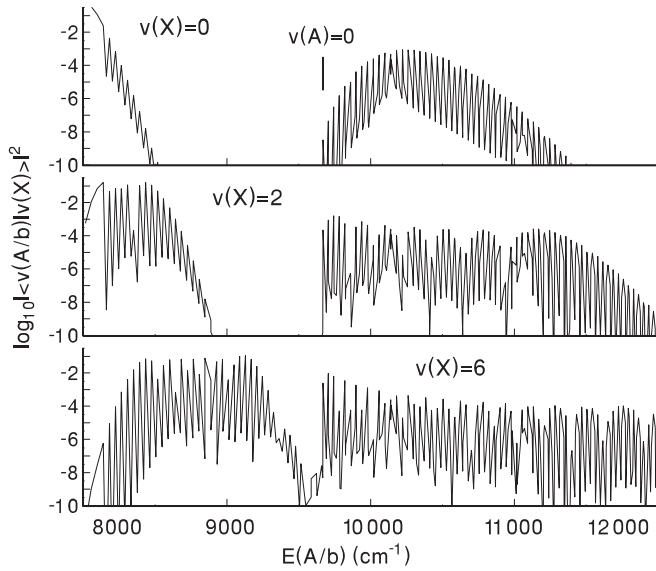


FIG. 15. Logarithm of the Franck-Condon factors for transitions between several levels of the $X^1\Sigma_g^+$ state to mixed A - b levels, for $J = 50$. Only the $A^1\Sigma_u^+$ part of the mixed wave function was used in the calculation.

Fluctuations in these FC factors are due to the varying fraction of $A^1\Sigma_u^+$ character. Analogous plots for different values of J are qualitatively similar once the energy scale is adjusted for the effects of centrifugal distortion.

Note in Fig. 15 that there are reasonably favorable FC factors from low levels of the $X^1\Sigma_g^+$ state to low levels of $b^3\Pi_{0u}^+$. For the X state, $r_e = 4.645 \text{ \AA}$, while for the $b0$ state, $r_e = 4.457 \text{ \AA}$ [50]. Because the r_e values are similar, the $v = 0$ wave functions overlap. Spin-orbit (ξ_{Ab0}^{SO}) mixes in some A -state character into the $v = 0$ level of $b^3\Pi_{0u}^+$, producing a significant $(b0 - X)(0,0)$ FC factor, as shown in Fig. 15. For higher vibrational levels of $b^3\Pi_{0u}^+$, the overlap with $X(v = 0)$ is less. This pattern is repeated for higher v of the X state, but extending over more v levels of $b^3\Pi_{0u}^+$. The FC factors increase again when the upper state energy approaches $v = 0$ of the $A^1\Sigma_u^+$ state. Thus in Fig. 15, there are in general two regions of appreciable FC factors, with a gap between them.

As noted above, one remarkable aspect of the transitions observed in Innsbruck from $X(v \sim 73)$ to A - b state levels was that the upper level of the strongest transitions often was primarily triplet in character, as judged by the calculated rotational structure or the fractional composition. This behavior was predicted by *ab initio* calculations [86], as well as by calculations with fitted potentials and DVR wave functions. Figure 16 shows the contrasting behavior in transitions between X -state levels and mixed A - b levels, depending on whether A - b character is dominant. Figure 17 shows that a small admixture of $A^1\Sigma_u^+$ character, with the correct phase, can produce a significant Franck-Condon overlap even for a level that is predominantly $b^3\Pi_{0u}^+$ in character. Thus the levels that have predominantly b state character are preferred as intermediate levels in the four-photon STIRAP scheme [12–14] because they give a much stronger transition on the first leg of the second two-photon transition and a more

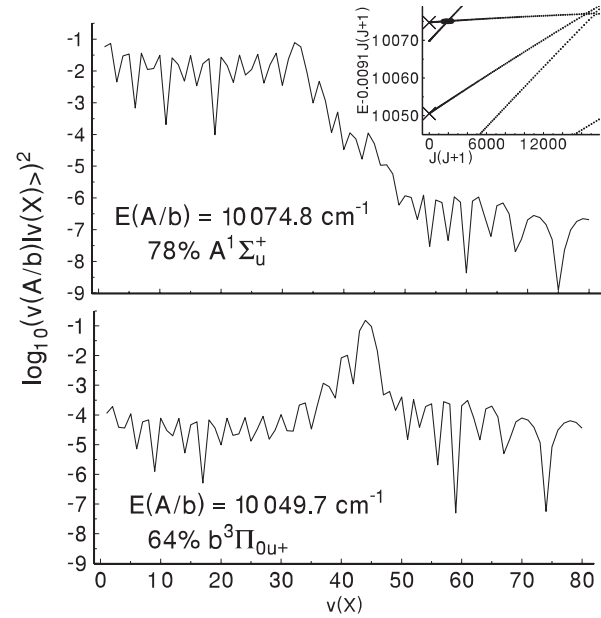


FIG. 16. Logarithm of the Franck-Condon factors for transitions between two nearby A - b levels to a range of levels of the $X^1\Sigma_g^+$ state, showing contrasting behavior. The inset shows that the level at 10049.7 cm^{-1} has a slope with $J(J + 1)$ characteristic of mostly $b^3\Pi_{0u}^+$ character, while the level at 10074.8 cm^{-1} has a slope with $J(J + 1)$ characteristic of mostly $A^1\Sigma_u^+$ character.

balanced distribution of transition strengths than levels of predominantly A character.

VI. CAN HYPERFINE STRUCTURE BE OBSERVED?

Hyperfine structure (hfs) was not observed in the experiments reported here, even though A - b states of Na_2 exhibited hyperfine structure of several hundred MHz [37] (in a regime in which the fraction of $b^3\Pi_{2u}$ character was significant), and the 6^2S Fermi contact splitting in Cs is 9192.63 MHz , as compared

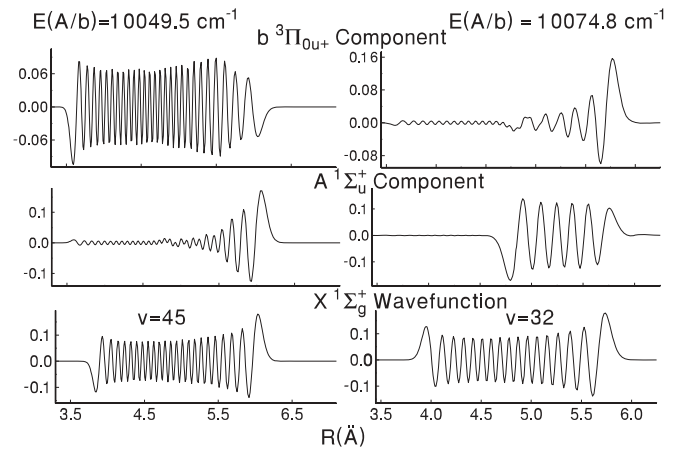


FIG. 17. Wave functions for the excited states in the previous figure, together with wave functions for the X -state levels that give the maximum Franck-Condon overlap with the A -state component. Although the level at 10049.7 cm^{-1} is mostly $b^3\Pi_{0u}^+$ character, it is intermixed with A -state character to give a substantial Franck-Condon factor for a transition from $X(v = 45)$.

with the Na 3^2S hfs splitting of 1771.616 MHz [87]. Since the OODR polarization technique with narrow-band lasers is inherently Doppler-free, one might ask why hfs has not been observed in the present work. Furthermore, the capability of exciting alkali-metal dimers from ultracold ground states or from Feshbach resonances, either of which are produced from cooled atoms, should also lead to possibilities for observing hyperfine structure with negligible Doppler width, in the lowest excited states of these species. With these questions in mind, we present a review of available information and then make some estimates of possible magnitudes of hyperfine structure.

A. Hamiltonian matrix elements

A detailed theory of hfs in molecular $^3\Pi$ states was developed in [88], and applied to molecular beam observations of the $a^3\Pi$ state of ^{13}CO [89,90]. Reference [89] translated the parameters of [88] into the more common notation of [91]. Reference [90] corrected errors in the Hamiltonian matrix of [89] and also in the forms adapted from [91]. An alternative formalism developed by [92], originally intended for application to the I_2 molecule, was applied to the $b^3\Pi_u$ state of Na_2 by [37]. Later, Ref. [93], from observations of the $1^3\Delta_g$ state of Na_2 , and Ref. [94], from data on mixed $A^1\Sigma_u^+$ and $b^3\Pi_u$ states of Na_2 , found that their observations could be explained almost entirely by the Fermi-contact parameter alone. Other studies of hfs in alkali-metal dimers, with one exception noted below, have found the Fermi contact parameter sufficient. However, we will present the Hamiltonian matrix elements for all the magnetic dipole parameters, neglecting possible contributions from electric quadrupole terms.

In terms of the hyperfine parameters defined in [95], (similar to the parameters of [91], but with $b_F = b + c/3$), plus two more parameters, d and e , not defined in these references, the elements of the magnetic dipole hfs operator are

$$\begin{aligned} \langle ^3\Pi_{0u\pm} | H_{MD} | ^3\Pi_{1u} \rangle &= (y/3)(x/2)^{1/2}(c \mp d - 3b_F), \\ \langle ^3\Pi_{1u} | H_{MD} | ^3\Pi_{1u} \rangle &= ya, \\ \langle ^3\Pi_{1u} | H_{MD} | ^3\Pi_{2u} \rangle &= (y/3)[(x-2)/2]^{1/2}(c - 3b_F), \\ \langle ^3\Pi_{1u} | H_{MD} | ^1\Sigma_u^+ \rangle &= yx^{1/2}e, \\ \langle ^3\Pi_{2u} | H_{MD} | ^3\Pi_{2u} \rangle &= 2y(a + b_F + 2c/3), \end{aligned} \quad (12)$$

where

$$\begin{aligned} x &= J(J+1); \\ y &= \frac{[F(F+1) - J(J+1) - I(I+1)]}{2J(J+1)}; \\ \vec{F} &= \vec{J} + \vec{I}. \end{aligned} \quad (13)$$

a , b_F , and c are the nuclear spin-orbital angular momentum interaction, the Fermi-contact interaction, and the electron spin-nuclear spin dipolar interaction. d and e are two additional dipole interaction terms, proportional, respectively, to D_{11} and D_{01} in [94] and [37].

Below, following [95], we define the parameters used above and, in the second equality, translate them to the parameters used by [37] and [94]. Here $\zeta = g_S g_N \mu_B \mu_N (\mu_0/4\pi)$, where $g_S(\mu_B)$ and $g_N(\mu_N)$ are the electron and nuclear g factors (Bohr magneton and nuclear magneton), respectively, and μ_0

is the vacuum permeability. Sums below are over the electrons, i , and nuclei, α :

$$\begin{aligned} a &= \sum_{i,\alpha} (2/g_S) \zeta \langle \Lambda = 1 | 1/r_{i,\alpha}^3 | \Lambda = 1 \rangle = G_{11}/2, \\ b_F &= \sum_{i,\alpha} \zeta \left(\frac{8\pi}{3} \right) \langle \Lambda = 1 | \delta(r_{i,\alpha}) | \Lambda = 1 \rangle = \left(\frac{K_{11}}{2\sqrt{6}} \right), \\ c &= \sum_{i,\alpha} \frac{3}{2} \zeta \langle \Lambda = 1 | (3 \cos^2 \theta_{i,\alpha}^2 - 1) / r_{i,\alpha}^3 | \Lambda = 1 \rangle = \left(\frac{D_{11}}{8\sqrt{5}} \right), \\ d &= \sum_{i,\alpha} \frac{3}{2} \zeta \langle \Lambda = -1 | e^{-2i\phi_{i,\alpha}} \sin^2 \theta_{i,\alpha} / r_{i,\alpha}^3 | \Lambda = 1 \rangle, \\ e &= \dots = \left(\frac{D_{10}}{8\sqrt{15}} \right). \end{aligned} \quad (14)$$

For e , the expression in terms of $\theta_{i,\alpha}$ and $r_{i,\alpha}$, while straightforward, is too lengthy to give here.

B. Estimate of splitting from the Fermi contact and other terms

If we write the Fermi contact term as $H_{\text{FmC}} = b_F \vec{I} \cdot \vec{S}$, then from [93] and [94], one obtains $b_F \sim A_{\text{hf,atom}}/4$, where $A_{\text{hf,atom}}$ is the atomic 2S hyperfine parameter. For the Cs 6^2S state, $A_{\text{hf,atom}} = 2298.16$ MHz [87]. Hence the molecular parameter, $b_F \sim 574.5$ MHz.

As in [37], we will designate a mixed 0_u^+ state by

$$|0_u^+\rangle = c_0|0\rangle + c_1|1\rangle + c_2|2\rangle + c_\Sigma|\Sigma\rangle, \quad (15)$$

where 0, 1, 2 denote $^3\Pi_{\Omega,u}$ states with $\Omega = 0, 1, 2$, and Σ denotes the $A^1\Sigma_u^+$ state.

Let us consider a state that is nominally $^3\Pi_{0u}$. Considering the Hamiltonian matrix elements in Eqs. (2), there will be some degree of $^3\Pi_1$ admixture, which we can estimate as

$$c_1 = \frac{\sqrt{2x}B}{E(^3\Pi_1) - E(^3\Pi_0)} \sim \frac{\sqrt{2x}B}{\xi_{b10}^{\text{SO}}}. \quad (16)$$

Considering only terms in b_F and letting $\hat{F} = F(F+1)$, etc., the hyperfine shifts of this nominal $^3\Pi_0$ state become

$$\begin{aligned} \langle 0_u^+ | H_{MD} | 0_u^+ \rangle &= -\frac{xyBb_F}{\xi_{b10}^{\text{SO}}} \sim \frac{[\hat{F} - \hat{J} - \hat{I}]Bb_F}{2\xi_{b10}^{\text{SO}}} \\ &\sim 20[\hat{F} - \hat{J} - \hat{I}]\text{kHz}, \end{aligned} \quad (17)$$

assuming $B \sim 1 \times 10^{-2} \text{ cm}^{-1}$ and $\xi_{b10}^{\text{SO}} \sim 150 \text{ cm}^{-1}$. For $J = 0$, the result is 0. In general, $F = |I - J| \dots (I + J)$. For given J , the maximum value of the expression in brackets is $2JI$, and thus for $I = 7$ (the maximum I value for Cs_2), the maximum value of this term is $\sim 280J$ kHz. In reality, most $^3\Pi_{0u}$ state levels of interest will be mixed with $A^1\Sigma_u^+$, so this estimate should be taken as an upper limit.

Thus, although splitting of the Cs atomic 6^2S state is 9.2 GHz, hyperfine shifts from the Fermi contact term in Cs_2 0_u^+ A - b states of low J are less than one MHz, due to the relatively large fine structure splitting in Cs_2 . Alternatively, one can say that for $\Omega = 0$ and $\Omega = 1$, the electron spin precesses rapidly around the internuclear axis, thereby reducing terms in $\vec{I} \cdot \vec{S}$.

To our knowledge, only one other hfs term besides the Fermi contact term has been convincingly determined in alkali-metal

dimer states and that is the c term, which was found to vary from zero to 9% b_F in various vibrational levels of the $c^3\Sigma^+$ state of NaK [96] (the many fitted parameters of [37] must be reviewed in light of the conclusions of [94]). From Eqs. (12), the c term would affect the observed hfs shifts to a fraction comparable to that reported by [96]. If $^3\Pi_{1u}$ levels of Cs₂ happen to be observed in cold molecule spectroscopy, then because the $\langle ^3\Pi_{1u} | H_{MD} | ^3\Pi_{1u} \rangle$ element is diagonal, the term in a might be detected. If a were also $\sim 5\%$ of b_F , shifts could be several MHz.

VII. CONCLUSIONS

In the interest of providing a model of the A - b state potentials and energy level structure for use in the experiments directed to the production of cold molecules, we have made use of data from several sources, obtained for various purposes, as noted above. Because the data are relatively sparse in certain regions, the analysis has required special procedures.

Questions that warrant further study have been noted above. For example, it appeared that some of the $b^3\Pi_{0u-}$ (f parity) low-vibrational levels, from the data of [51], could better be assigned to $^3\Pi_{2u}$. As laser techniques improve, it would be interesting to attempt to access these levels with high resolution techniques. Secondly, the second-order

spin-orbit (SO2) corrections to the $b^3\Pi_{1u}$ potential are quite large, and sensitively dependent on the relative potentials of perturbing states, as shown in Fig. 5. More extensive data on $b^3\Pi_{1u}$ levels might shed light on these SO2 corrections. And finally, as discussed in Sec. VI, it remains a challenge to observe hyperfine structure in levels with substantial $b^3\Pi_{2u}$ character. This also would require enhanced laser techniques, such as used recently to study $B^1\Pi_u \rightarrow X^1\Sigma_g^+$ transitions in Cs₂ [57].

ACKNOWLEDGMENTS

The work in Temple University was supported by NSF grant no. PHY-0855502. S.K. acknowledges support from AFOSR and from NSF grant no. PHY-1005453. S.A., C.M., and J.H. were supported by NSF grants no. PHY-0652938 and PHY-0968898. The work at Stony Brook was supported by NSF grants no. PHY-0652459 and PHY-0968905. The work in Tsinghua University was supported by NSFC of China, under grant no. 20773072. The Moscow team thanks the Russian Foundation for Basic Researches by the grant no. 10-03-00195 and MSU Priority Direction 2.3. M.T. and R.F. are grateful to Ilze Klincare, Olga Nikolayeva, and Artis Kruzins for their help in spectra analysis, as well as appreciate the support from the ESF 2009/0223/1DP/1.1.1.2.0/09/APIA/VIAA/008 project.

-
- [1] See, for example, L. Li and A. M. Lyyra, *Spectrochim. Acta A* **55**, 2147 (1999) on the use of window states to excite higher triplet states of Li₂ and Na₂.
- [2] J. M. Sage, S. Sainis, T. Bergeman, and D. DeMille, *Phys. Rev. Lett.* **94**, 203001 (2005).
- [3] J. Deiglmayr, A. Grochola, M. Repp, K. Mörtilbauer, C. Glück, J. Lange, O. Dulieu, R. Wester, and M. Weidemüller, *Phys. Rev. Lett.* **101**, 133004 (2008).
- [4] S. Ospelkaus, A. Pe'er, K.-K. Ni, J. J. Zirbel, B. Neyenhuis, S. Kotochigova, P. S. Julienne, J. Ye, and D. S. Jin, *Nature Physics* **4**, 622 (2008).
- [5] K.-K. Ni, S. Ospelkaus, M. H. G. de Miranda, A. Pe'er, B. Neyenhuis, J. J. Zirbel, S. Kotochigova, P. S. Julienne, D. S. Jin, and J. Ye, *Science* **322**, 231 (2008).
- [6] K. Aikawa, D. Akamatsu, M. Hayashi, K. Oasa, J. Kobayashi, P. Naidon, T. Kishimoto, M. Ueda, and S. Inouye, *Phys. Rev. Lett.* **105**, 203001 (2010).
- [7] C. Haimberger, J. Kleinert, P. Zabawa, A. Wakim, and N. P. Bigelow, *New J. Phys.* **11**, 055042 (2009).
- [8] F. Lang, K. Winkler, C. Strauss, R. Grimm, and J. Hecker Denschlag, *Phys. Rev. Lett.* **101**, 133005 (2008).
- [9] C. M. Dion, C. Drag, O. Dulieu, B. Laburthe-Tolra, F. Masnou-Seeuws, and P. Pillet, *Phys. Rev. Lett.* **86**, 2253 (2001).
- [10] M. Viteau, A. Chotia, M. Allegrini, N. Bouloufa, O. Dulieu, D. Comparat, and P. Pillet, *Science* **321**, 232 (2008).
- [11] J. G. Danzl, E. Haller, M. Gustavsson, M. J. Mark, R. Hart, N. Bouloufa, O. Dulieu, H. Ritsch, and H.-C. Nägerl, *Science* **321**, 1062 (2008).
- [12] M. J. Mark *et al.*, *Appl. Phys. B* **95**, 219 (2009).
- [13] J. G. Danzl, M. J. Mark, E. Haller, M. Gustavsson, N. Bouloufa, O. Dulieu, H. Ritsch, R. Hart, and H.-C. Nägerl, *Faraday Discuss.* **142**, 283 (2009).
- [14] J. G. Danzl, M. J. Mark, E. Haller, M. Gustavsson, R. Hart, J. Aldegunde, J. M. Hutson, and H.-C. Nägerl, *Nature Physics* **6**, 265 (2010).
- [15] A. Derevianko, *Phys. Rev. A* **67**, 033607 (2003).
- [16] D. DeMille, S. Sainis, J. Sage, T. Bergeman, S. Kotochigova, and E. Tiesinga, *Phys. Rev. Lett.* **100**, 043202 (2008); see also T. Zelevinsky, S. Kotochigova, and J. Ye, *ibid.* **100**, 043201 (2008).
- [17] W. C. Stwalley, *Eur. Phys. J. D* **31**, 221 (2004).
- [18] C. Lisdat, O. Dulieu, H. Knöckel, and E. Tiemann, *Eur. Phys. J. D* **17**, 319 (2001).
- [19] M. Tamanis, R. Ferber, A. Zaitsevskii, E. A. Pazyuk, A. V. Stoloyarov, H. Chen, J. Qi, H. Wang, and W. C. Stwalley, *J. Chem. Phys.* **117**, 7980 (2002).
- [20] M. R. Manaa, A. J. Ross, F. Martin, P. Crozet, A. M. Lyyra, L. Li, C. Amiot, and T. Bergeman, *J. Chem. Phys.* **117**, 11208 (2002).
- [21] T. Bergeman, C. E. Fellows, R. F. Gutterres, and C. Amiot, *Phys. Rev. A* **67**, 050501 (2003).
- [22] P. Qi *et al.*, *J. Chem. Phys.* **127**, 044301 (2007).
- [23] O. Docenko, M. Tamanis, R. Ferber, E. A. Pazyuk, A. Zaitsevskii, A. V. Stoloyarov, A. Pashov, H. Knöckel, and E. Tiemann, *Phys. Rev. A* **75**, 042503 (2007).
- [24] J. Zaharova, M. Tamanis, R. Ferber, A. N. Drozdova, E. A. Pazyuk, and A. V. Stoloyarov, *Phys. Rev. A* **79**, 012508 (2009).

- [25] A. Kruzins, I. Klincare, O. Nikolayeva, M. Tamanis, R. Ferber, E. A. Pazyuk, and A. V. Stolýarov, *Phys. Rev. A* **81**, 042509 (2010).
- [26] M. Tamanis, I. Klincare, A. Kruzins, O. Nikolayeva, R. Ferber, E. A. Pazyuk, and A. V. Stolýarov, *Phys. Rev. A* **82**, 032506 (2010).
- [27] O. Docenko, M. Tamanis, R. Ferber, T. Bergeman, S. Kotochigova, A. V. Stolýarov, A. deFaria Nogueira, and C. E. Fellows, *Phys. Rev. A* **81**, 042511 (2010).
- [28] A. J. Ross, C. Effantin, J. d’Incan, and R. F. Barrow, *Mol. Phys.* **56**, 903 (1985).
- [29] A. J. Ross, C. Effantin, J. d’Incan, and R. F. Barrow, *J. Phys. B* **19**, 1449 (1986).
- [30] A. J. Ross, R. M. Clements, and R. F. Barrow, *J. Mol. Spectrosc.* **127**, 546 (1988).
- [31] H. Sun and J. Huennekens, *J. Chem. Phys.* **97**, 4714 (1992).
- [32] R. Ferber, E. A. Pazyuk, A. J. Stolýarov, A. Zaitsevskii, H. Chen, H. Wang, and W. C. Stwalley, *J. Chem. Phys.* **112**, 5740 (2000).
- [33] X. Xie and R. W. Field, *Chem. Phys.* **99**, 337 (1985).
- [34] X. Xie and R. W. Field, *J. Mol. Spectrosc.* **117**, 228 (1986).
- [35] C. Linton, F. Martin, I. Russier, A. J. Ross, P. Crozet, S. Churassy, and R. Bacis, *J. Mol. Spectrosc.* **175**, 340 (1996).
- [36] K. Urbanski, S. Antonova, A. M. Lyyra, A. Yiannopoulou, and W. C. Stwalley, *J. Chem. Phys.* **104**, 2813 (1996).
- [37] J. B. Atkinson, J. Becker, and W. Demtröder, *Chem. Phys. Lett.* **87**, 92 (1982).
- [38] C. Effantin, O. Babaky, K. Hussein, J. d’Incan, and R. F. Barrow, *J. Phys. B* **18**, 4077 (1985).
- [39] H. Katô, M. Otani, and M. Baba, *J. Chem. Phys.* **89**, 653 (1988).
- [40] A. M. Lyyra, H. Wang, T.-J. Whang, W. C. Stwalley, and L. Li, *Phys. Rev. Lett.* **66**, 2724 (1991).
- [41] T.-J. Whang, W. C. Stwalley, L. Li, and A. M. Lyyra, *J. Chem. Phys.* **97**, 7211 (1992).
- [42] A. J. Ross, P. Crozet, C. Effantin, J. d’Incan, and R. F. Barrow, *J. Phys. B* **20**, 6225 (1987).
- [43] A. M. Lyyra, W. T. Luh, L. Li, H. Wang, and W. C. Stwalley, *J. Chem. Phys.* **92**, 43 (1990).
- [44] G. Jong, PhD thesis, University of Iowa, 1991 (unpublished).
- [45] G. Jong, L. Li, T.-J. Whang, A. M. Lyyra, W. C. Stwalley, M. Li, and J. Coxon, *J. Mol. Spectrosc.* **155**, 115 (1992).
- [46] J. T. Kim, H. Wang, C. C. Tsai, J. T. Bahns, W. C. Stwalley, G. Jong, and A. M. Lyyra, *J. Chem. Phys.* **102**, 6646 (1995).
- [47] C. Amiot, O. Dulieu, and J. Vergès, *Phys. Rev. Lett.* **83**, 2316 (1999).
- [48] H. Salami *et al.*, *Phys. Rev. A* **80**, 022515 (2009).
- [49] J. Vergès and C. Amiot, *J. Mol. Spectrosc.* **126**, 393 (1987).
- [50] C. Amiot and O. Dulieu, *J. Chem. Phys.* **117**, 5155 (2002).
- [51] F. Xie, D. Li, L. Tyree, L. Li, V. B. Sovkov, V. S. Ivanov, S. Magnier, and A. M. Lyyra, *J. Chem. Phys.* **128**, 204313 (2008).
- [52] See supplemental material at [<http://link.aps.org/supplemental/10.1103/PhysRevA.83.032514>]. The supplemental material consists of fitted parameters, numerical listings for potentials, spin-orbit functions and second-order spin-orbit functions, X state term values, observed and fitted $A - b$ term values, pump transitions used at Temple University, LIF series observed at LAC, and Franck-Condon factors. See [<http://www.aip.org/pubservs/epaps.html>].
- [53] J. A. Coxon and P. G. Hajigeorgiou, *J. Chem. Phys.* **132**, 094105 (2010).
- [54] R. Teets, R. Feinberg, T. W. Hänsch, and A. L. Schawlow, *Phys. Rev. Lett.* **37**, 683 (1976).
- [55] M. Raab, G. Höning, W. Demtröder, and C. R. Vidal, *J. Chem. Phys.* **76**, 4370 (1982).
- [56] X. Wang, J. Magnes, A. M. Lyyra, A. J. Ross, F. Martin, P. M. Dove, and R. J. Le Roy, *J. Chem. Phys.* **117**, 9339 (2002).
- [57] N. Nishimiya, Y. Yasuda, T. Yukiya, and M. Suzuki, *J. Mol. Spectrosc.* **255**, 194 (2009).
- [58] C. Wolfe, PhD thesis, Lehigh University, 2010 (unpublished).
- [59] C. Wolfe, S. Ashman, B. Beser, E. H. Ahmed, J. Bai, A. M. Lyyra, and J. Huennekens, accepted for publication in *J. Chem. Phys.* (2011).
- [60] J. Derouard, *Chem. Phys.* **84**, 181 (1984). We thank D. Pritchard and R. W. Field for alerting us to this reference.
- [61] W. Demtröder, *Laser Spectroscopy* (Springer, Berlin, 2008), Vol. 2.
- [62] S. Kasahara, Y. Hasui, K. Otsuka, M. Baba, W. Demtröder, and H. Katô, *J. Chem. Phys.* **106**, 4869 (1997).
- [63] Karl Lambrecht Corporation, Chicago, IL.
- [64] D. Skinner and R. Whitcher, *J. Phys. E* **5**, 237 (1972).
- [65] The Aimé Cotton Iodine Atlas, S. Gerstenkorn and P. Luc, Atlas du Spectre d’Absorption de la Molecule d’Iode, Editions du CNRS, Paris, 1978, was recalibrated in 1979 by S. Gerstenkorn and P. Luc, *Rev. Phys. Appl.* **14**, 791 (1979).
- [66] H. Salami and A. J. Ross, *J. Mol. Spectrosc.* **223**, 157 (2005).
- [67] B. A. Palmer, R. A. Keller, and R. Engleman Jr., “An atlas of uranium emission intensities in a hollow cathode discharge,” LASL Rep. LA-8251-MS (Los Alamos Scientific Laboratory, Los Alamos, NM, 1980).
- [68] J. Y. Seto, R. Le Roy, J. Vergès, and C. Amiot, *J. Chem. Phys.* **113**, 3067 (2000).
- [69] R. W. Field and H. Lefebvre-Brion, *The Spectra and Dynamics of Diatomic Molecules* (Elsevier, Amsterdam, 2004).
- [70] E. G. Lee, J. Y. Seto, T. Hirao, P. F. Bernath, and R. J. Le Roy, *J. Mol. Spectrosc.* **194**, 197 (1999).
- [71] R. J. Le Roy, Y. Huang and C. Jary, *J. Chem. Phys.* **125**, 164310 (2006); R. J. Le Roy and R. D. E. Henderson, *Mol. Phys.* **105**, 663 (2007).
- [72] D. A. Steck, Cesium D Line Data (2009) [<http://steck.us.alkalidata>].
- [73] H. M. Hulburt and J. O. Hirschfelder, *J. Chem. Phys.* **9**, 61 (1941).
- [74] N. Spies, PhD thesis, Fachbereich Chemie, Universität Kaiserslautern.
- [75] M. Dolg, in *Effective Core Potentials*, published in Modern Methods and Algorithms of Quantum Chemistry, edited by J. Grotendorst (John von Neumann Institute for Computing, Jülich, 2000), NIC Series, Vol. 1, pp. 479–508 [<http://www.fz-juelich.de/nic-series/>].
- [76] P. J. Knowles and H.-J. Werner, *Theor. Chim. Acta* **84**, 95 (1992).
- [77] W. Müller, J. Flesch, and W. Meyer, *J. Chem. Phys.* **80**, 3297 (1984).
- [78] H.-J. Werner *et al.*, MOLPRO, version 2008.1, a package of *ab initio* programs, see [www.MOLPRO.net].
- [79] A. Zaitsevskii, E. A. Pazyuk, A. V. Stolýarov, O. Docenko, I. Klincare, O. Nikolayeva, M. Auzinsh, M. Tamanis, and R. Ferber, *Phys. Rev. A* **71**, 012510 (2005).
- [80] I. S. Lim, P. Schwerdtfeger, B. Metz, and H. Stoll, *J. Chem. Phys.* **122**, 104103 (2005).

- [81] H.-J. Werner and P. J. Knowles, *J. Chem. Phys.* **82**, 5053 (1985).
- [82] P. A. Malmqvist, A. Rendell, and B. Roos, *J. Phys. Chem.* **94**, 5477 (1990).
- [83] S. Kotochigova and E. Tiesinga, *J. Chem. Phys.* **123**, 174304 (2005).
- [84] P. Moroshkin, A. Hofer, V. Lebedev, and A. Weis, *J. Chem. Phys.* **133**, 174510 (2010).
- [85] R. P. Benedict, D. L. Drummond, and L. A. Schlie, *J. Chem. Phys.* **70**, 3155 (1979).
- [86] N. Bouloufa and O. Dulieu (unpublished).
- [87] E. Arimondo, M. Inguscio, and P. Violino, *Rev. Mod. Phys.* **49**, 31 (1977).
- [88] K. Freed, *J. Chem. Phys.* **43**, 4214 (1966).
- [89] R. Gammon, R. Stern, M. Lesk, B. Wicke, and W. Klemperer, *J. Chem. Phys.* **54**, 2136 (1971).
- [90] R. Saykally, T. Dixon, T. Anderson, P. Szanto, and R. C. Woods, *J. Chem. Phys.* **87**, 6423 (1987).
- [91] R. A. Frosch and H. M. Foley, *Phys. Rev.* **88**, 1337 (1952).
- [92] M. Broyer, J. Vigué, and J. C. Lehmann, *J. de Physique* **39**, 591 (1978).
- [93] L. Li, Q. Zhu, and R. W. Field, *J. Mol. Spectrosc.* **134**, 50 (1989).
- [94] H. Katô, M. Otani, and M. Baba, *J. Chem. Phys.* **91**, 5124 (1989).
- [95] J. Brown and A. Carrington, *Rotational Spectroscopy of Diatomic Molecules* (Cambridge University Press, Cambridge, 2003).
- [96] P. Kowalczyk, *J. Chem. Phys.* **91**, 2779 (1989).